POLITECNICO DI TORINO

Master's Degree
in Electronic Engineering

Master's Degree Thesis

Tin oxide nanowire sensors: fabrication process simulation and electrical modeling

Supervisor
Prof. Gianluca Piccinini
Co-Supervisors
Ph.D. Fabrizio Mo
Ph.D. Chiara Elfi Spano

Candidate
Rosario Enrico Stimolo

July 2022

To my family

Summary

During the last decades, many fields (e.g., from disease diagnostics to environmental monitoring and from industrial process control to safety systems) have had increased demand for highly sensitive, small size and portable gas-sensing devices.

In this scenario, metal-oxide based chemiresistive gas sensors, which responses depend on the change in their electrical conductance upon interaction with the target gas, have been widely studied and commercialized. Tin oxide (SnO_2) is one of the widely used and most important metal-oxide semiconductor used in gas sensors mainly due to its sensitivity to different gaseous species. Metal oxide nanowires have demonstrated improved properties compared to the conventional thick film gas sensors mainly due to their huge surface-to-volume ratio, which leads to improved gas response.

The first part of this work is a literature review of the metal oxide gas sensors. Metal oxide semiconductors, general gas-sensing mechanisms and fabrication processes of metal oxides nanowires gas sensors are introduced as well as the vapor – liquid – solid growth method and RF magnetron sputtering and lift-off for the bottom-up and top-down fabrication process approaches, respectively.

The second part is instead focused on the simulation of the fabrication process of a tin oxide nanowire gas sensor based on the top-down approach. Sentaurus Process and Sentaurus Topography 3D were used for the process simulation while Sentaurus Device was used for the electrical simulation.

Acknowledgements

I would like to thank my supervisor, Prof. Gianluca Piccinini, for his valuable teachings throughout the bachelor and master's degree courses and for having aroused in me a great interest in the technology field.
I would also like to thank my co-supervisors, Ph.D. Fabrizio Mo and Ph.D. Chiara Elfi Spano, for their useful advice and for the support they gave me during my thesis work.

Contents

List of Tables

List of Figures

Part I

First Part

Chapter 1

Introduction

Currently the requirements to improve quality of life and public safety are dramatically increasing due to issues related to the air pollution and the development of different industry sectors. Hence, there is a great interest in portable gas sensing technologies to provide real-time monitoring of outdoor and indoor air quality. Moreover, the detection of volatile organic compounds is an effective way to perform medical diagnostics and food quality control. In general, chemiresistive gas sensor devices based on semiconducting metal oxides have attracted great attention and have a wide range of applications, some examples are:

- Detection and quantification of environmentally hazardous gases.
- Automotive emission monitoring.
- Aerospace-vehicle health monitoring.
- Industrial process control.
- Safety systems.
- Human health diagnostics.
- Food quality control.
- Detection of explosive and toxic gaseous compounds.

Over the past decades, several kinds of gas sensors have been developed based on various transduction platforms and different sensing materials. Among all the different sensing materials, chemiresistive semiconducting metal oxides are the most potential candidates due to:

- Very low cost.
- High sensitivity.
- Fast response/recovery time.

- Simple electronic interface.
- Ease of use.
- Low maintenance.
- Ability to detect large number of gases.

Tin oxide (SnO_2) is one of the most important and widely used metal-oxide semiconductors used in gas sensors mainly due to its sensitivity to different gaseous species.
Miniaturization of the sensing device leads to many advantages, mainly intrinsically higher response and lower power consumption. Among the several different nanostructures that, recently, have been produced and that have been considered to be an effective sensor fundamental building block, the nanowire structure is advantageous mainly due to its huge surface-to-volume ratio and, as a consequence, improved gas response.
A resistive metal-oxide nanowire sensor uses surface chemical reactions and subsequent changes in its conductivity (change in the density of conduction band electrons or valence band holes) for gas sensing.

1.1 Modeling and simulation route

Sensors stability, sensitivity and selectivity has always been a prime design concern for gas sensors designers. Modeling and simulation of gas sensors aids the designers in improving their performance and enables the sensor designers in understanding the sensing mechanism. Moreover, it aids sensor designers in deciding the structure and its parameters for achieving maximum performance [12].

Figure 1.1. Simulation path for gas sensors. Steady state response is for illustration only and the computational package mentioned is proprietary software.

As shown in figure 1.1 the gas sensing response can be obtained by defining the sensor structure and material properties in Sentaurus TCAD and considering the steady state surface bending which may lead to the sensor's steady state response [12].
A device based on a tin oxide nanowire on a Si/SiO_2 substrate with Ti/Au contacts is the object of this work. The complete fabrication process was simulated using Sentaurus Process and Sentaurus Topography 3D; the last one allows to simulate advanced deposition

process such as physical vapor deposition, which is the method chosen for the SnO_2 deposition. Finally, the electrical behaviour of the structure, generated after the fabrication process simulation, is simulated using Sentaurus Device.

Chapter 2

Semiconducting metal oxide as gas sensors

Metal oxides form an important class of chemical compounds in which oxygen is combined with a metal. Their maximum of valence band and minimum of conduction band chiefly consist of the oxygen 2p and metal ns orbital, respectively. Semiconducting metal oxides are valence compounds with a high level of ionic bonding. Due to their electronic charge transport properties chemiresistive semiconducting metal oxides have exclusive material characteristics when compared to conventional covalent semiconductors like silicon or germanium [10].

2.1 Environmentally hazardous gases

Environmentally hazardous gases include green house gases such as N_2O, CH_4 and CO_2, toxic gases such as H_2S, CO and NH_3 and special gases such as NO_2, NO and SO_2, which are both green house gases and toxic. Table 2.1 summarizes the threshold limit value (TLV) of the gases mentioned up to now [18].

Chemical formula	IUPAC name	TLV
NO_2	Nitrogen dioxide	3 ppm
NO	Nitric oxide	25 ppm
N_2O	Nitrous oxide	50 ppm
H_2S	Hydrogen sulfide	10 ppm
CO	Carbon monoxide	50 ppm
NH_3	Ammonia	25 ppm
CH_4	Methane	1000 ppm
SO_2	Sulfur dioxide	5 ppm
CO_2	Carbon dioxide	5000 ppm

Table 2.1. Threshold limit value (TLV) of environmentally hazardous gases.

The need to establish threshold limit values derives from the fact that both living and working environments are often exposed to chemical agents, which, even if minimal, can have serious effects on health. Threshold limit value (TLV) is defined as the maximum concentration of a chemical allowable for repeated exposure without producing adverse health effects.
Based on oxidizing and reducing effects, environmentally hazardous gases can be divided into two groups. H_2S, CO, NH_3, CH_4 and SO_2 are reducing gases whereas NO_2, NO, N_2O and CO_2 are oxidizing gases. When the n-type sensing material is heated in clean air, oxygen in air is adsorbed on the sensing material and attracts free electrons, causing increase in the sensor resistance, resulting in less flow of electrons inside the sensing material. In the presence of reducing gases, the reducing gas reacts with adsorbed oxygen and the electrons held by adsorbed oxygen are released into the sensing material. As a result, sensor resistance decreases, allowing more current. In the presence of oxidizing gases, sensor resistance increases.

2.2 Metal oxide semiconductors

Over the past decades, various kinds of gas sensors based on different sensing materials have been developed. The main types of gas-sensing materials include conducting polymer composite, metal-oxide semiconductors, metal-oxide/polymer composite, intrinsically conducting polymer and other novel materials [18].
Chemiresistive semiconducting metal oxides are some of the most potential candidates due to simple electronic interface, ability to detect large number of gases, ease of use, very low cost, low maintenance, fast response time, fast recovery time and high sensitivity [18].

2.2.1 n-type and p-type semiconducting metal oxide

The two main types of semiconducting metal oxide sensors are n-type and p-type. Just like silicon semiconductors, for n-type metal oxide the majority carrier is electron while for p-type the majority carrier is hole.
Because electrons are naturally produced via oxygen vacancies, majority of semiconducting metal oxides are n-type. Oxygen vacancies, which are pervasive in metal oxides, can be considered as point defects and these intrinsic point defects serve as the donors or acceptors. When the band gaps of metal oxides are wide and the defect levels are too deep to provide high concentration carriers, extrinsic doping is needed to realize moderate or high conductivity. However, in the following only intrinsic metal oxides are considered [10], [18].
Sensing materials based on SnO_2 are used by most the companies. SnO_2 is by far the most investigated gas sensing material, with NO_2, CO and volatile organic compounds (VOC) being the principal target gases; WO_3 is the second most investigated material. Most of the experimental and theoretical information has been gathered on SnO_2, and all modelling of, for example, sensing and transduction, has been concentrated on the n-type case [1].

Table 2.2 summarizes some examples of semiconducting metal oxides as sensors for environmentally hazardous gases.

Type	Metal oxides	Majority carrier	Minority carrier
n-type	Zinc oxide, tin dioxide, titanium dioxide, iron(III) oxide, etc.	Electron	Hole
p-type	Nickel oxide, cobalt oxide, chromium(III) oxide and few others	Hole	Electron

Table 2.2. Examples of n-type and p-type semiconducting metal oxides.

2.3 General gas-sensing mechanisms

2.3.1 Adsorption

Since the word "adsorbed" has been used several times in this context it is worth defining what adsorption means. Adsorption is the adhesion of atoms, ions or molecules from a gas, liquid or dissolved solid to a surface. This process forms an adsorbate film on the surface of the adsorbent. This process differs from absorption, which occurs when a fluid (the absorbate) is dissolved by or permeates a liquid or solid (the absorbent). The term sorption encompasses both processes, while desorption is the reverse of it. Adsorption is a surface phenomenon, whereas absorption affects the entire volume of the substance, although adsorption does often precede absorption. Adsorption, like surface tension, is a consequence of surface energy. In a bulk material, all the bonding requirements (be they ionic, covalent or metallic) of the constituent atoms of the material are fulfilled by other atoms in the material. However, because atoms on the surface of the adsorbent are not completely surrounded by other adsorbent atoms, they can attract adsorbates. The exact nature of the bonding depends on the details of the species involved, but the adsorption process is commonly classified as physisorption (characteristic of weak van der Waals forces) or chemisorption (characteristic of covalent bonding) [19].

2.3.2 Gas-sensing mechanisms

The basic oxide gas sensor is deceptively simple, consisting essentially of an insulating substrate with electrode metallization on one side and a heater on the other. The hard ceramic form of gas sensitive stannic oxide is put across the electrode and heated to a temperature suitable for operation via the substrate, at which point its resistance reaches an equilibrium value. When a detected gas arrives, a change in resistance occurs, which

is measured by an electronic circuit, which then operates an alarm or displays the gas concentration. There are two types of gas sensing oxides: bulk- and surface-sensitive materials. TiO_2 is classified as a bulk sensitive gas sensing material because it increases its conductivity as a result of the creation of bulk oxygen vacancies under reducing circumstances. SnO_2, on the other hand, is classified as a surface sensitive material despite the fact that bulk defects affect its conductivity. Because of the dispersing conduction band with its minimum at the C-point and the high mobility of charge carriers, a small change in charge carrier concentration results in a large change in the electrical conductance of the material. As a result, adsorbate-induced band bending has the potential to cause a significant change in electrical conductivity in this material, triggering a gas response signal. In TiO_2, however, the band gap is indirect with the conduction band minimum not at the C-point. As a result, band bending does not have a significant impact on its electrical conductivity [20]. On the following the general gas-sensing mechanisms of metal oxides is analyzed.
In the presence of clean air, oxygen is absorbed on the metal oxide surface. The sensing material is heated by the heater at several hundred °C; with the heater situated on the reverse side of the sensing material surface. The surface reactions proceed to slowly to be useful at lower temperatures. The adsorption of oxygen produces ionic species including O^{2-}, O^- and O_2^-, which have acquired electrons from the conduction band of the metal oxide. The oxygen ions O^{2-}, O^- and O_2^- are stable above 300°C, between 100 and 300°C and below 100°C, respectively. The adsorption kinematics are explained by the following reaction paths [18]:

$$O_2(gas) \Leftrightarrow O_2(absorbed) \tag{2.1}$$

$$O_2(absorbed) + e^- \Leftrightarrow O_2^- \tag{2.2}$$

$$O_2^- + e^- \Leftrightarrow 2O^- \tag{2.3}$$

$$O^- + e^- \Leftrightarrow O^{2-} \tag{2.4}$$

Oxygen vacancies act as preferential adsorption sites for gas molecules. It results in trapping or extracting electrons from the conduction band which causes the change of resistivity. The more oxygen vacancies are generated, the higher is the gas sensitivity, as higher concentration of gas molecules can be adsorbed [9].
The electron concentration in the sensing material decreases as electrons transfer from the conduction band to the chemisorbed oxygen. An increase in the resistance of the metal oxide is observed for n-type semiconducting metal oxide. On the contrary, the resistance of p-type metal oxide is reduced.
When the metal oxide surface is exposed to reducing gases, the reducing gas reacts with the chemisorbed oxygen and the electrons held by chemisorbed oxygen are released back to the conduction band of the sensing material. The overall reducing reactions between the reducing gases and the chemisorbed O^{2-} and O^- are given by [18]:

$$2NH_3 + 3O^-(ads) \rightarrow N_2 + 3H_2O + 3e^- \tag{2.5}$$

$$2NH_3 + 3O^{2-}(ads) \rightarrow N_2 + 3H_2O + 6e^- \tag{2.6}$$

$$H_2S + 3O^-(ads) \rightarrow H_2O + SO_2 + 3e^- \tag{2.7}$$

$$H_2S + 3O^{2-}(ads) \rightarrow H_2O + SO_2 + 6e^- \tag{2.8}$$

$$CO + O^-(ads) \rightarrow CO_2 + e^- \tag{2.9}$$

$$CO + O^{2-}(ads) \rightarrow CO_2 + 2e^- \tag{2.10}$$

$$SO_2 + O^-(ads) \rightarrow SO_3 + e^- \tag{2.11}$$

$$SO_2 + O^{2-}(ads) \rightarrow SO_2 + 2e^- \tag{2.12}$$

$$CH_4 + 4O^-(ads) \rightarrow 2H_2O + CO_2 + 4e^- \tag{2.13}$$

$$CH_4 + 4O^{2-}(ads) \rightarrow 2H_2O + CO_2 + 8e^- \tag{2.14}$$

As a title of example in figure 2.1 is reported a metal oxide gas sensor, SnO_2 for this particular case, in the presence of air at first and then in the presence of ethanol, which is a reducing gas.

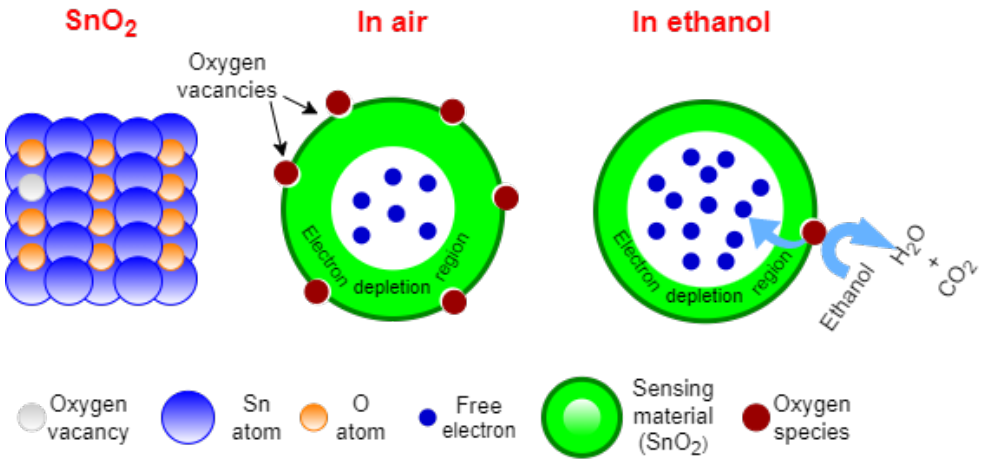

Figure 2.1. Sensing mechanism for SnO_2 in air and ethanol.

When the metal oxide surface is exposed to oxidizing gases, the oxidizing gas reacts with the adsorbed O^- ions as well as adsorb directly on the metal oxide surface. The overall oxidizing reactions between the oxidizing gases and the metal oxide are given by [18]:

$$NO_2(gas) + e^- \rightarrow NO^{2-}(ads) \tag{2.15}$$

$$NO^{2-}(ads) + O^-(ads) + 2e^- \rightarrow NO(gas) + 2O^{2-}(ads) \tag{2.16}$$

$$NO(gas) + e^- \rightarrow NO^-(ads) \tag{2.17}$$

$$2NO^-(ads) \rightarrow N_2(gas) + 2O^-(ads) \tag{2.18}$$

$$N_2O(gas) + e^- \rightarrow N_2O^-(ads) \tag{2.19}$$

$$N_2O^-(ads) \rightarrow N_2(gas) + O^-(ads) \tag{2.20}$$

$$CO_2(gas) + e^- \rightarrow CO^{2-}(ads) \tag{2.21}$$

$$CO^{2-}(ads) + O^-(ads) + 2e^- \rightarrow CO(gas) + 2O^{2-}(ads) \tag{2.22}$$

The adsorption of oxygen species represents a very interesting step in metal oxide gas sensors, because the oxygen species assist the adsorbed oxidizing ions to take electrons from the metal oxide surface. For reducing gases, on the other hand, the oxygen species assist the adsorbed reducing ions to give electrons to the metal oxide surface [18].

2.3.3 Tin oxide gas-sensing mechanisms

The principle of operation lies on the fact that the electrical conductivity changes experienced by an n-type material when surface chemisorbed oxygen reacts with reducing gases are detected by SnO_2-based sensors. Because conduction electrons are bound to surface oxygen in clean air, the conductivity of SnO_2 is low; however, in the presence of a reducing gas, electrons are no longer bound to the surface states, and the conductivity increases. As a result, the surface resistance of SnO_2 is controlled by gaseous species adsorption. The band structures of SnO_2 vary in air due to oxygen molecule adsorption. The periodicity of the crystal structure is broken at the surface, resulting in unsaturated sites or dangling bonds. In this example, the oxygen molecule picks up electrons from the surface of SnO2, and the charge transfer equation is [20]:

$$\beta/2O_2(g) + \alpha e^- \Leftrightarrow O_\beta^{-\alpha} \tag{2.23}$$

Where alpha can be one or two depending on the oxygen reduction states, and beta can be one for single atom/ionic form and two for molecular form of oxygen. The creation of a space charged layer at the surface occurs from the charge transfer process between

atmospheric oxygen and the SnO_2 surface. An electric field is generated by the net charge at the surface, which causes a bending of the energy bands in SnO_2. A negative surface charge bends the bands upward, i.e. pushes the Fermi levels in the band gap of SnO_2, effectively reduce the charge carrier concentration and resulting in an electron depletion zone. In other words, this is an electron trapping mechanism at the surface that causes the surface layer electrical resistance to increase (or conductivity to decrease). When a reducing molecular gas adsorbs at its surface, electrons can be transferred to these molecules if the lowest unoccupied molecular orbitals of the adsorbate lie below the Fermi levels (acceptor levels) of SnO_2 and vice versa electrons are donated to SnO_2 if the highest occupied molecular orbitals lie above the Fermi levels of the SnO_2 (donor levels). When a reducing gas, such as CO, reacts with the adsorbed oxygen to form CO_2, which can be expressed by the following oxidation reaction [20]:

$$\beta CO(g) + O_{\beta}^{-\alpha} \rightarrow \beta CO2(g) + \alpha e^{-} \tag{2.24}$$

The electrons released in this reaction are injected into the SnO_2 conduction band, causing the electrical resistance to decrease (or increase in conductivity). Figure 2.2 depicts the creation of the depletion region by oxygen adsorption and the reduction of the depletion region by reducing gas adsorption [20].

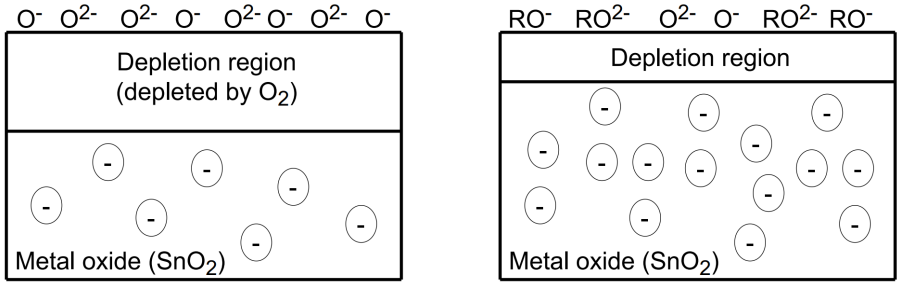

Figure 2.2. Tin oxide sensor in clean air (left) and in presence of reducing agent (right).

In reality, the reducing gas removes oxygen ions from SnO_2 surfaces, which are then replenished from the atmosphere and becomes available for further reaction. As a result, the reaction rates of gas oxidation and oxygen ion replacement dictate the presence of an equilibrium density of oxygen ions. The conductivity of SnO_2 is defined by this equilibrium density of oxygen ions, which is dependent on the partial pressure on the reducing gas in the atmosphere. This also clarifies why SnO_2 sensors exhibit different sensitivities to different gases, having different oxidation rates, and variation of sensitivity as well as the response and recovery times with operation temperatures, since oxidation rate is a function of temperature [20].

Polycrystalline tin oxide

The sensor signal for SnO_2 will be based only on changes in surface conductivity. In practice, however, the oxygen ion species occupy only about 2% of the surface area of SnO_2 (in

the case of a single crystalline surface). This is due to the fact that adsorption takes place only on those defects which make the phenomenon of chemisorption possible. Therefore, the mechanism of gas sensing may be insufficient to account for a large sensitivity actually measured for several gases. When the polycrystalline structures of SnO_2 are considered, the mechanisms leading to substantial resistance changes can be explained. This structure is essentially an agglomeration of SnO_2 crystallites, each of which is an n-type semiconductor with oxygen lattice defects acting as electron donors at the grain boundaries. As a result, when oxygen atoms are dissociated to produce ionic species that adsorb on the surface of crystallites, electrons are removed from SnO_2, resulting in space charge layers with their concomitant potential barriers. Therefore, the heights of these barriers depend upon the equilibrium concentration of adsorbed oxygen. Adsorbed oxygen species react with reducing gases to lower potential barrier heights, resulting in a significant reduction in resistance. This method suggests that SnO_2 in the nanocrystalline form will greatly improve sensitivity to various gases, and in fact, nanocrystalline structures are currently the focus of international gas sensor research.

2.3.4 Gas-sensing response

The gas-sensing response is an important parameter that allows to quantify the relationship between the electrical resistance of the sensor in pure dry air and the electrical resistance of the sensor in the presence of reducing/oxidizing gases [18].
In the presence of reducing gases, the concentration of electrons on the surface of metal oxide increases and the resistance of n-type metal oxide decreases correspondingly. On the contrary, the resistance of p-type metal oxide surface increases since generated electrons recombine with holes, decreasing the hole concentration.
By defining R_a and R_{rg} as the electrical resistances of the sensor measured in the presence of pure dry air and reducing gas, respectively, the gas-sensing responses for n-type (S^n_{rd}) and p-type (S^p_{rd}) semiconducting metal oxide to reducing gas are defined as [18]:

$$S^{n}_{rd} = \frac{R_a}{R_{rg}} \tag{2.25}$$

$$S^{p}_{rd} = \frac{R_{rg}}{R_a} \tag{2.26}$$

In the presence of oxidizing gases, the concentration of electrons on the surface of metal oxide decreases and the resistance of n-type metal oxide increases correspondingly. On the contrary, the resistance of p-type metal oxide surface decreases since extracted electrons result in generation of holes in the valence band.
By defining R_a and R_{og} as the electrical resistances of the sensor measured in the presence of pure dry air and oxidizing gas, respectively, the gas-sensing responses for n-type (S^n_{ox}) and p-type (S^p_{ox}) semiconducting metal oxide to oxidizing gas are defined as [18]:

$$S^{n}_{ox} = \frac{R_{og}}{R_a} \tag{2.27}$$

$$S^{p}{}_{ox} = \frac{R_a}{R_{og}} \tag{2.28}$$

At the temperature range of 250-350°C the response of the sensor is high due to adsorbed oxygen species. However, the dominant process becomes the adsorption of oxygen ions as the temperature increases, then the response of the sensor decreases. Moreover, at very high temperature range, progressive desorption of all species occurs and the response decreases. In conclusion, the gas-sensing response for semiconducting metal oxide sensors increases as the temperature increases till it reaches a maximum after which, as the temperature still increases, decreases [18].
Table 2.3 summarizes how the electrical conductivity of semiconducting metal oxide changes under exposure of reducing/oxidizing gases.

Semiconducting metal oxide	Reducing gas	Oxidizing gas
n-type	Resistance decreases	Resistance increases
p-type	Resistance increases	Resistance decreases

Table 2.3. Electrical conductivity changing of semiconducting metal oxide under exposure of reducing and oxidizing gases.

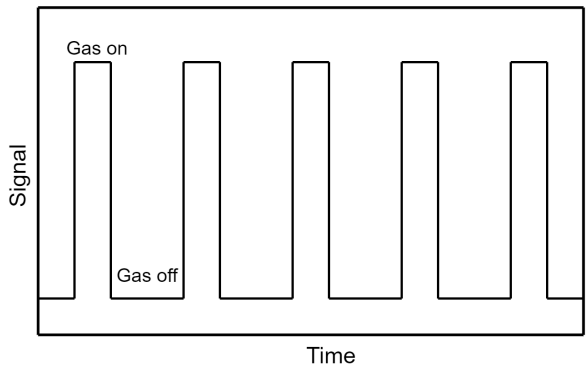

Figure 2.3. Typical response curve of a gas sensor.

When exposed to the molecules of the analysing gas, the electrical resistance of a chemiresistive sensor varies dramatically (increases or decreases). The type of the sensor material and the gas determine how the resistance increases or decreases. A typical gas sensor response curve with time on exposure and withdrawal of the analysing gas is schematically depicted in figure 2.2. The response curve of a sensor is characterized by following six parameters: sensitivity, response time, recovery time, selectivity, long term stability, and reproducibility.
Response and recovery times, in addition to response, can be used to describe the gas-sensing features of metal oxide semiconductors. The time it takes to reach 90% of the

steady response signal is commonly referred to as the response time. On the other hand, the time required to recover 90% of the original baseline resistance is commonly referred to as the recovery time [18].

Chapter 3

Metal oxide nanowires gas sensors

Researchers have been interested in nanomaterials for a long time, but among the various morphologies described in the literature, nanowires (NWs) related ones offer higher material quality as well as outstanding design freedom. These are the properties that make nanowires structures capable of propelling materials engineering and fundamental science forward. The ability to control material composition at a nanometric level is extremely relevant, especially for semiconducting materials. Furthermore, with nanowires, lattice matching for epitaxy is not a significant constraint because the eventual strain can easily relax along a nanometer-scale interface. Furthermore, the numerous possibilities and freedom in designing the shape and morphology allowed with nanowires can open novel and innovative material combinations and configurations. We can exploit also nanowires exceptional flexibility, when dealing with them. Because nanowires are so small, they are incredibly robust and tough and they can withstand massive mechanical deformations without breaking or fracturing. It is possible to make various and peculiar assemblies on flexible substrates to develop high performances biocompatible, flexible, wearable sensors for the detection of chemical compounds, human health, environmental air quality, and food quality monitoring. The mechanical flexibility together with the large aspect ratio of nanowires allow their processability through various techniques such as spin coating, drop casting and roll printing [4].
Although the basic gas sensing mechanism (adsorption and desorption of gas molecules) remains the same, nanowire gas sensors and sensor arrays have a number of unique qualities when compared to traditional flat-film sensors [3].

Low power consumption, light weight and wireless communication capability
Nanowire sensors are important for long range coverage since they have minimize size, light weight and consume less power. Advanced gas sensor and wireless communication capabilities can be accomplished with nanowires, for example via distributed ad-hoc sensor networks, allowing for long range guidance of all kinds of gas detection.

Fast response time and ultra sensitivity Nanowires gas sensors exhibit ultra sensitivity and fast response time. A few gas molecules are enough to modify the electrical characteristics of the sensing elements due to their small size and high surface-to-volume ratio. This enables the detection of a very low gas concentration in a matter of seconds.

Low-temperature operations The electrical properties of nanowires may be changed by very small volumes of gas, allowing the sensors to operate at lower temperatures.

3.1 Fabrication processes of metal oxides nanowires gas sensors

There are two basic approaches to synthesizing nanowires: top-down and bottom-up. The two approaches are still applied even today after so many years of research in this area and the advantages and disadvantages of these approaches are reviewed. A top-down approach uses numerous methods, such as lithography, to reduce a large piece of material to small pieces. The bottom-up approach, on the other hand, builds up through smart use of self-assembly the desired structures. Figure 3.1 highlights the difference between the bottom-up approach and the top-down approach.

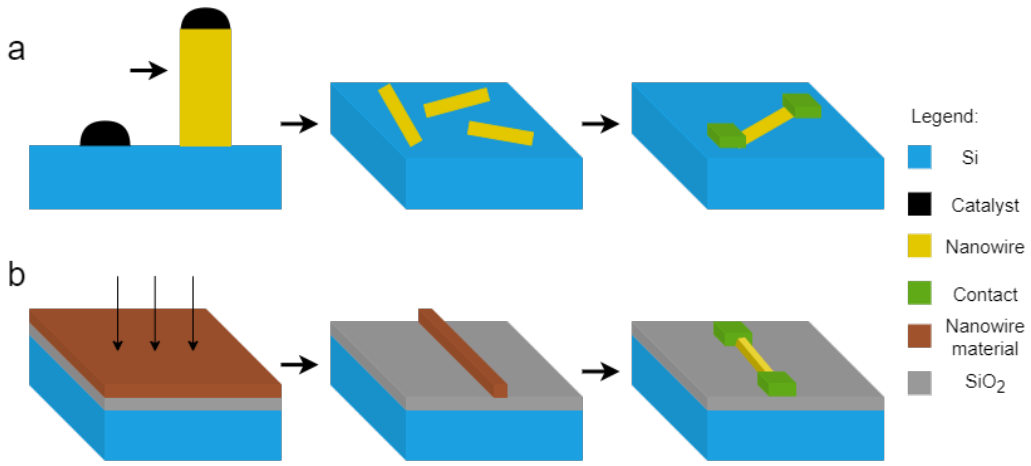

Figure 3.1. The nanowire sensors fabricated using (a) the bottom-up approach and (b) the top-down approach.

3.1.1 Bottom-up versus top-down

Top-down approach starts with patterns made on a large scale while reducing the lateral dimensions to the nanoscale. The top-down approach – as developed in the fabrication of integrated circuits – has the advantage of allowing the parts to be patterned and

built in place, eliminating the need for an assembly step. Another advantage is that well-ordered structures with great homogeneity in nanowire diameters and lengths are easier to obtain. The challenge with all top-down strategies is that, while they function well at the microscale, implementing them in nanoscale dimensions becomes progressively difficult. However, top-down techniques work good in the range of 100 nm – 10 μm. Moreover, they involve planar techniques, which involve the addition and subtraction of patterned layers to produce the structures (deposition and etching). As a result, constructing arbitrary three-dimensional objects is difficult. Despite the fact that lithographic techniques are commercially viable and frequently used in manufacturing, these top-down approaches are afflicted by expensive equipment costs, especially when fabricating high-resolution structures [3].
Table 3.1 summarizes the pros and cons of the top-down approach.

Advantages of top-down approach	Drawbacks of top-down approach
No assembly step is needed	Increasingly difficult to implement in nanoscale dimensions
Easier to obtain well-ordered structures, with high homogeneity in nanowire diameters and lengths	Arbitrary three-dimensional objects are difficult to construct
Lithographic techniques are commercially viable and widely utilized in manufacturing	High equipment costs

Table 3.1. Advantages and drawbacks of top-down approach.

The bottom-up approach, on the other hand, starts with individual atoms and molecules and builds up, in some cases through smart use of self-assembly, the desired nanostructures. The majority of synthesis techniques use a bottom-up approach. Bottom-up approaches have the important advantage of being able to generate structures with diameters ranging from angstroms to hundreds of nanometers. Another benefit is that nanowires can be formed on almost any type of surface, including those that are normally incompatible with standard CMOS processing, such as flexible plastic substrates. A further advantage is that sequential patterning and assembly steps enable fabrication of distinct nanowire devices on a substrate. However, building hierarchical structures only by bottom-up self-assembling processes may be very difficult. A successful outcome cannot yet be obtained by sole reliance on the bottom-up concept with the current state of self-assembly science. In fabricating the required structures in practical applications, positioning of assembled patterns on specific locations is particularly difficult [3].
Table 3.2 summarizes the pros and cons of the bottom-up approach.
The integration of top-down and bottom-up approaches is expected to eventually provide the best combination of tools for nanofabrication as shown in Figure 3.2. A growing number of studies have shown that combining top-down and bottom-up techniques helps speed up the development of complex applications. It has been stated that such a combination can build cost-effective nanostructures [3].

Thus, from a scientific standpoint, we now require both techniques for many nanowire-related applications.

Advantages of bottom-up approach	Drawbacks of bottom-up approach
Nanowires can be assembled on nearly any type of surface	Positioning of assembled patterns on specific locations is difficult in fabricating the required structures
Sequential patterning and assembly steps enable fabrication of distinct nanowire devices on a substrate	Difficult construction of hierarchic structures

Table 3.2. Advantages and drawbacks of bottom-up approach.

Some of the synthesis techniques of both the bottom-up and top-down approaches are summarized in table 3.3.

Approach	Fabrication methods
Top-down	Optical and X-ray lithography, e-beam and ion-beam lithography, printing and imprinting, scanning probe lithography, etc.
Bottom-up	Vapor-liquid-solid (VLS) growth, chemical vapour deposition (CVD), sol-gel processing, plasma or flame spraying synthesis, laser pyrolysis, atomic or molecular condensation, layer-by-layer self assembly, molecular self assembly, coating and growth, direct assembly, etc.

Table 3.3. Fabrication methods of top-down and bottom-up approaches.

Finally, there are different strategies to enhance the chemical sensing performances of metal oxide nanowires. The addition of noble metals is a well-known and well-studied technique for tailoring chemical sensing performance, but more recently, the insertion of catalysts has been proposed, with synergetic effects demonstrated. In addition to catalyzation, surface functionalization and heterostructures formation, doping has been effectively used to tune chemical sensing performances [4].

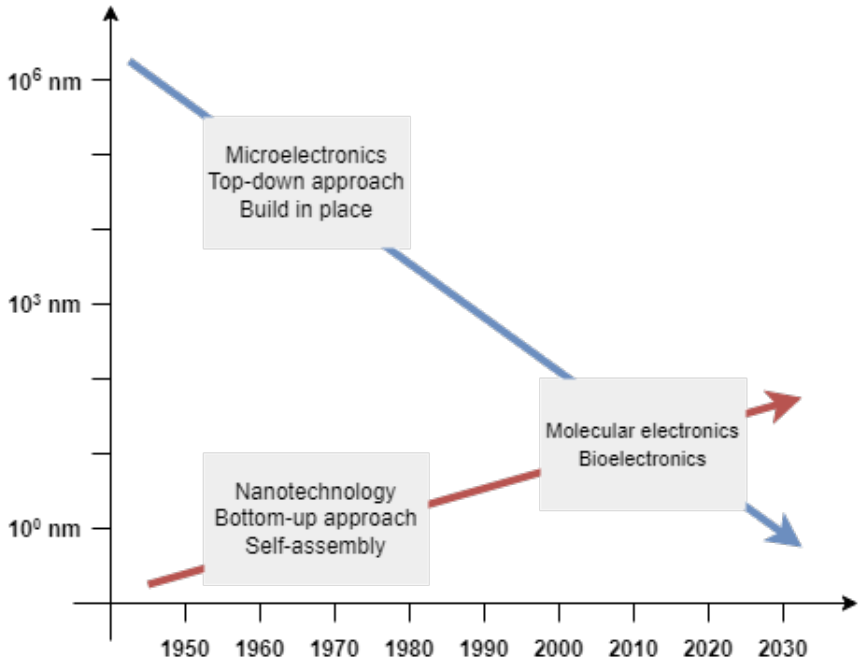

Figure 3.2. Evolution of bottom-up and top-down approaches.

3.2 Vapor – Liquid – Solid growth method

The growth mechanism at the base of the majority of nanowire preparation experimental procedures is vapor-liquid-solid (VLS) as it may be exploited for a wide class of materials and structures. The vapor–liquid–solid method is a mechanism for the growth of one-dimensional structures, such as nanowires, from chemical vapor deposition. All three phases are involved in this particular method, this is why it is called vapor–liquid–solid method.
In figure 3.3 the overall process is reported.
The substrate is the material on which we want the growth to happen on. On the solid substrate there is a liquid catalyst droplet composed from a different material than the substrate. The catalyst is purposely introduced and forms a liquid droplet by itself or by alloying with growth material during the growth. The growth species is evaporated first and then diffuses and dissolves into the liquid droplet. The catalyst acts as a trap for the growth species. Thus, the gas particles imping the liquid catalyst droplet and then, as the supersaturation reaches, we get precipitation at the interface of the solid and the liquid droplet. As more and more particles come onto the liquid droplet and precipitate the column starts moving; growth species in the catalyst droplets subsequently precipitates at the growth surface resulting in the one-directional growth. Note that at the tip there is the liquid droplet which initially was on top of the substrate. The growth direction is controlled by the droplet which is on the tip of the nanorod that starts to form. The

dimension of the liquid droplet fixes the diameter of the nanorod; hence for a small diameter of the droplet we get a thin nanowire while for a large diameter of the droplet we get a thick nanowire.

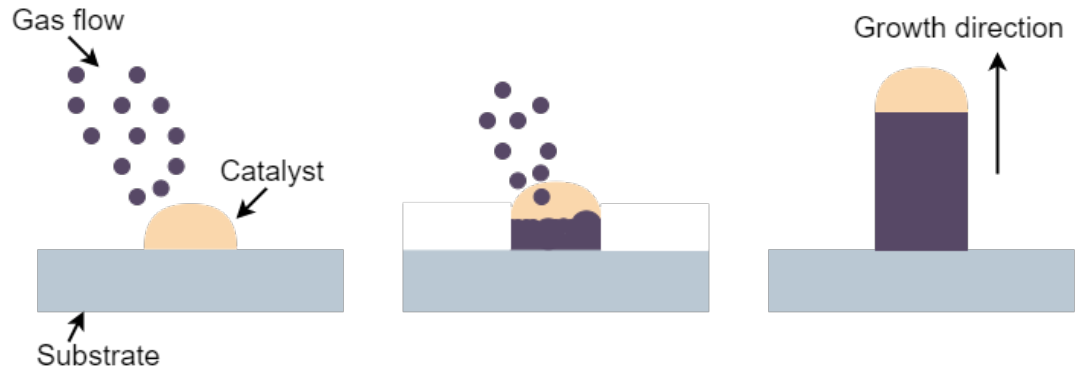

Figure 3.3. Vapor liquid solid growth.

On the following we will go into detail by breaking it down this whole process into small steps.

3.2.1 Requirements for VLS growth

Some fundamental requirements stand at the basis of the vapor–liquid–solid mechanism for the growth of one-dimensional nanowires.

Liquid catalyst droplet The catalyst or the impurity must form a liquid droplet with the crystalline material to be grown at the decomposition temperature.

Catalyst distribution coefficient The distribution coefficient[1] of the catalyst or impurity must be less than unity at decomposition temperature.

Catalyst equilibrium vapor pressure The equilibrium vapor pressure[2] of the catalyst over the liquid droplet must be small: evaporation reduces the diameter of the droplet which ultimately will reduce the diameter of the nanowire. This means that the catalyst should not be evaporating very quickly.

Inert catalyst Catalyst should be chemically inert. The catalyst should not react with the growth material.

[1] In the physical sciences, a partition coefficient or distribution coefficient is the ratio of concentrations of a compound in a mixture of two immiscible solvents at equilibrium.

[2] The equilibrium vapor pressure is defined as the pressure exerted by a vapor in thermodynamic equilibrium with its condensed phases (solid or liquid) at a given temperature in a closed system. The equilibrium vapor pressure is an indication of a liquid's evaporation rate.

Wetting angle (interfacial energy) Wetting[3] characteristic (interfacial energy) of the catalyst influences the diameter of the nanowire. A small wetting angle results in large diameter.

Compound nanowire growth For a compound nanowire growth, one of the constituents can serve as the catalyst.

Controlled unidirectional growth For controlled unidirectional growth, the solid liquid interface must be well defined crystallographically; single crystals ideal as substrate.

3.2.2 Kelvin equation

The equilibrium vapor pressure or solubility is dependent on the surface energy and radius of the surface by Kelvin equation:

$$ln\frac{P}{P_0} = -\frac{2\gamma\Omega}{kTr} \ . \tag{3.1}$$

In (3.1) the various quantities have the following meanings:

- P : vapor pressure of the curved surface.
- P_0 : vapor pressure of the flat surface.
- γ : surface energy.
- Ω : atomic volume.
- r : surface radius.
- T : temperature.
- k : Boltzmann constant.

The gas particles must be soluble in the liquid droplet; this depends on the equilibrium vapor pressure that can be controlled by controlling the interfacial energy, the temperature and the radius of the droplet. All that will contribute to the equilibrium vapor pressure and will enhance or decrease the solubility of these particles in the liquid, this will ultimately control the amount of particles which are getting precipitated at the liquid-solid interface.

[3]Wetting is the ability of a liquid to maintain contact with a solid surface, resulting from intermolecular interactions when the two are brought together. This happens in presence of a gaseous phase or another liquid phase not miscible with the first one.

3.2.3 Reaction chamber

Nanowires growth by the VLS method can happen in a chemical vapor deposition system. It is possible to obtain nanostructures with precise sizes by modulating the deposition parameters, like plasma power and chamber pressure, to find the proper thermodynamic conditions for nucleation.
The reaction chamber consists of a horizontal quartz tube inside a horizontal furnace. The material (i.e. pure tin if we want to build SnO_2 nanowire) powder is placed in an alumina boat at the centre of the furnace as the evaporation source. The substrate (i.e. a piece of silicon wafer deposited with sputters of a thin film of gold acting as catalyst) is placed at each end of the alumina boat. The system is then pumped up to its pressure limit. Mass-flow controller and valves can control the gas inlet (i.e. argon, oxygen) and gas outlet [17].
In figure 3.4 the sketching picture of the CVD system is reported.

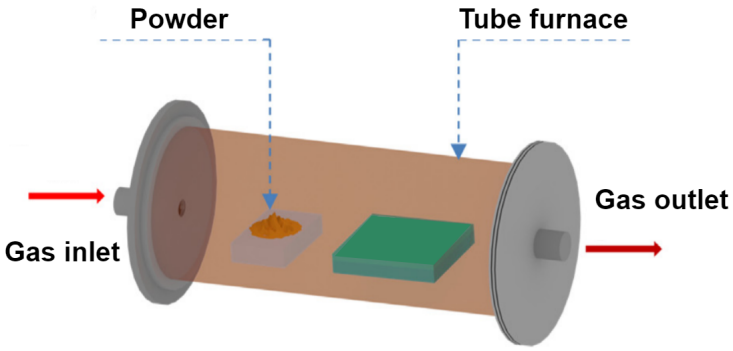

Figure 3.4. Sketching picture of the CVD system: material powder and substrate are placed in a quartz tube in furnace.

3.2.4 Thermal dewetting

On the substrate (i.e. a piece of silicon wafer) there must be a catalyst (i.e. a thin film, 2–5 nm, of gold deposited with sputtering). A metastable metal thin film where atoms are locked into their position due to kinetic barriers can be formed by vapor phase deposition of a high surface energy material (i.e. a metal) on a low surface energy substrate (i.e. an oxide). However, if the sample is heated immediately after deposition, the atoms will gather enough energy to overcome the remaining kinetic barriers, and the system will continue to progress toward equilibrium. This assembly method is known as thermal dewetting, and it is one of the most straightforward ways to make substrate-based metal nanoparticles; dewetting of thin metal layers leads towards nanoparticles respectively droplets.
Very high frequency fluctuations which are also very low amplitude (few nanometers). These fluctuations are attributed to the internal kinetic energy of the molecules. Every material has an internal energy which has several components, like internal potential

energy which is essentially the interaction forces like van der Waals forces, internal kinetic energy, etc. The internal kinetic energy of the molecules is numerically presented as k_BT, where T is absolute temperature and k_B is the Boltzmann constant. Note that this term is nonzero so whenever we see a stagnant free surface at room temperature (cup of coffee or bucket of water) there is some very high frequency low amplitude fluctuations. Thus, the molecules try to go away with each other and surface tension of the interaction forces bind them together. There is a competition that goes on and this leads to this type of fluctuations. These fluctuations are omni present (figure 3.5, phase 1), unless we are performing our experiment at absolute zero (figure 3.5, initial state).

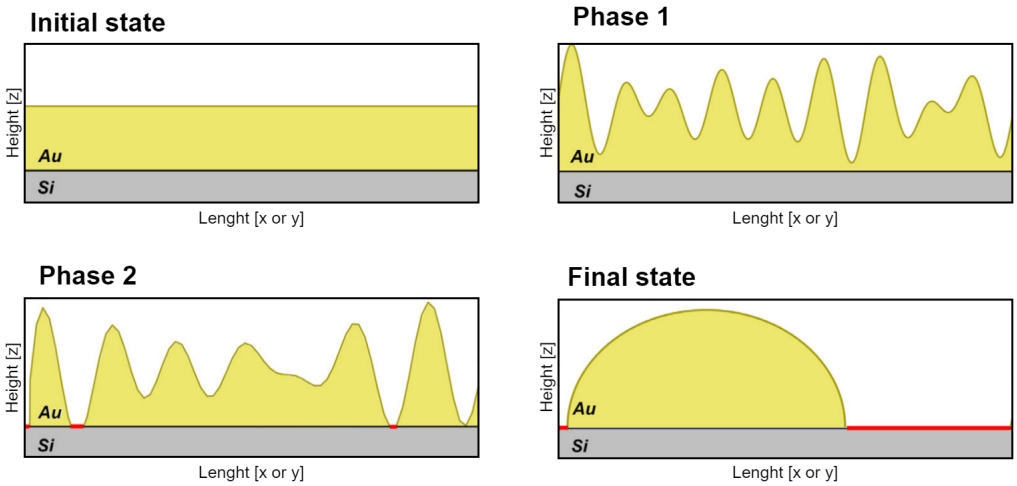

Figure 3.5. The four different states of spinodal dewetting.

If the film surface is flat that corresponds to the lowest surface energy configuration. The moment there is these fluctuations due to the internal kinetic energy or oscillation of the molecules, it increases the surface energy and surface tension opposes this growth. There is a dynamic steady state: fluctuation-flattening and so on. While these fluctuations are meaningless considering a bucket of water, if we think of a thin film (thickness of 100 nm or less) these fluctuations, that have amplitude of some nanometers, became important.
If the overall thickness of the film is lower than 100 nm there is active van der Waals interaction. In case the van der Waals interaction (interaction that scales as $1/d^2$, where d is the separation distance) is attractive, in figure 3.6 we can observe that at point 1 the van der Waals interaction is stronger than point 2. Thus, since the liquid free surface is a deformable surface, it deforms because it is feeling an attraction towards the surface of the substrate due to van der Waals force and this is what is called disjoining pressure.
On the other hand, Laplace pressure is responsible for a film flattening. Thus, there is a competition between Laplace pressure versus van der Waals force driven disjoining pressure. The destabilizing effect is due to van der Waals force or disjoining pressure and the stabilizing effect is by surface tension. In case the strength of this disjoining pressure is stronger than the Laplace pressure then the amplitude of the fluctuations will grow.

It will grow till the bottom of this fluctuation touches the substrate (amplitude matches film thickness), at this point the two interfaces (the free surface of the liquid and the liquid-solid interface) have merged to form a three phase contact line that is associated with the formation of a hole. The formation of hole is an indicator that the film has raptured. The film has ruptured with a very low value contact angle. Since a liquid on a solid system has a specific equilibrium contact angle given by Young's equation, the contact line will retract up to when this contact angle reaches the equilibrium contact angle. The retraction of the contact line on the solid surface is called dewetting.

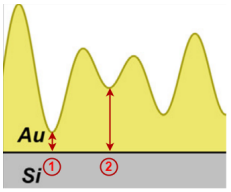

Figure 3.6. Van der Waals interaction at two different points.

Previous studies of the effective interfacial potential revealed that there are two plausible mechanisms: spinodal dewetting and induced dewetting [7].
The simplest case is induced dewetting, which occurs when a layer is disturbed or warped. Mechanical impact or a statistically random event causes a hole to form in the layer. This is where dewetting begins. As the hole expands, the material is piled up at the edge and pushed forward, generating droplets where the holes meet. The other mechanism is spinodal dewetting, which occurs when the thickness of a layer fluctuates, causing a large number of holes and droplets to form at the same time. There are four stages to spinodal dewetting (figure 3.5) leading to a final droplet state. The starting layer state depicts an undisturbed, uniform layer. In phase 1, the layer is heated, resulting in greater Brownian motion. The effective interfacial potential may amplify this movement, resulting in spatial oscillation or warping in layer thickness. In phase 1, these spatial oscillations are stable, but in phase 2, they become unstable. Here, the motion is increased even further, resulting in material wave valleys striking the underlying substrate. In this method, a hole is created in the layer, which expands in the same way that the induced mechanism's holes do. The primary distinction is that the holes in spinodal dewetting are generated in the sequence indicated by heat-induced warping increased by the effective interfacial potential, rather than randomly [7].
The resultant areal densities, sizes, crystal orientations and shapes are strongly influenced by the deposition and annealing conditions, impurities, film thicknesses and substrate parameters including orientation, crystal structure and surface texture.
The formation of catalyst droplet is a crucial step since it allows to control the dimension of the final nanowire structure.

3.2.5 Steps involved

Growth species is evaporated first, diffuses and dissolves into a liquid droplet. Surface of the liquid has large accommodation coefficient and is the preferred site of deposition. In any heterogeneous catalyst reaction involving a solid surface there are some sites the gas molecules preferably occupy but since this is a liquid droplet every site can accommodate the incoming gas molecules. Saturated growth species in the liquid droplet will diffuse to and precipitate at the interface between the substrate and the liquid (becomes supersaturated, the precipitation occurs). The growth should be carried out above the eutectic temperature of the catalyst and the reactant.
For growth of uniform high quality crystalline nanowires, super saturation should be kept low. Very high super saturation will lead to polycrystalline or amorphous nanorod formation. A high super saturation results in growth of other facets. Further increase in super saturation results in termination of growth.

3.3 RF magnetron sputtering and lift-off

The top-down approach uses lithographic techniques that are commercially viable and widely utilized in manufacturing to synthetize nanowires. On the following a top-down approach based on metal oxide deposition via RF magnetron sputtering and lift-off is analysed. Note that these two techniques (RF magnetron sputtering and lift-off) can be used to create the contacts.

3.3.1 RF magnetron sputtering

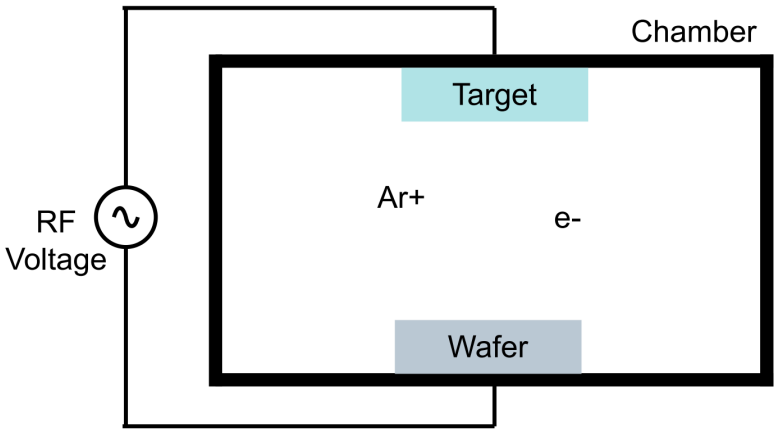

Figure 3.7. Sketching picture of the RF magnetron sputtering system: wafer and target are placed inside the reaction chamber which is connected to the RF voltage generator.

The RF magnetron sputtering technique is a physical vapor deposition (PVD) method of film deposition. If the material is taken in solid state, but sent as very small particles

or atoms and deposited on the wafer without any reaction we are talking about physical vapor deposition. Thus, atoms are moved and deposited on the substrate, differently from chemical vapor deposition where the gaseous molecules react with the substrate. The physical vapor deposition technique is best suited to coat in application that demand a tough cutting edge such as lift-off (for easier resist removal). Table 3.4 summarizes the major differences between physical vapor deposition and chemical vapor deposition.

	Physical Vapor Deposition	Chemical Vapor Deposition
Applications	PVD is used to make articles that require films for mechanical, optical, chemical or electronic functions. For example, semiconductor devices, thin-film solar panels, glass coatings, and etc.	CVD is used to produce high quality, high-performance solid materials. This process is commonly used in the semiconductor industry to produce thin films.
Temperature	Relatively low temperature (around 250°C - 450°C).	High temperatures in the range of 450°C to 1050°C.
Method	Atoms are moving and depositing on the substrate.	The gaseous molecules will react with the substrate.

Table 3.4. Comparison between physical vapor deposition and chemical vapor deposition.

The RF magnetron sputtering system is depicted in figure 3.7 where one can see the RF sputtering chamber, the target (which is the material we want to deposit), the wafer and the connecting wires to the supply RF voltage. Inside the chamber a plasma is formed, this is indicated by the Ar+ (argon ions) and the e- (electrons) symbols. The RF voltage is typically sinusoidal and remains positive for most of the time (i.e. remains positive for 75% of the period and negative for 25% of the period).
When considering the first half cycle, the positive terminal is connected to the wafer and the negative terminal to the target. Thus, the argon ions hit the target and deposit it to the wafer. However, some argon ions get stuck in the target surface form a positive charge layer. The back side of the target have negative charge but there will not be an electrical connection if the target is an insulator. Now argon ions are not able to hit the target due to positive charge layer. Electrons are the light particles and they hit the wafer with less force not causing damage to the sputtered layer. During the second half cycle, the positive terminal is connected to the target and the negative terminal to the wafer. In this case, electrons go to the target and remove the positive charge layer. Argon ions will not hit the wafer since the wafer remains negative for short time; even if argon ions hit the wafer they removes some of the material from the wafer and make it rough and this roughness will help the deposition on the next step.
Note that argon is used since it is an inert gas that will not react with the wafer or the target. Helium and neon can also be used but it is more difficult to ionize them and they are more expensive than argon.

To quantify the quality of the deposition one can define the sticking coefficient. The sticking coefficient is defined as the ratio of the number of atoms (or molecules) that "stick" to a surface to the total number of atoms that impinge upon that surface during the same period of time. If all the atoms that impinge upon that surface stick to it, then the sticking coefficient is 1; if none of the atoms that impinge upon that surface stick to it, then the sticking coefficient is 0. Typically, the sticking coefficient is about 0.7 or 0.8.
Note that because of the nonpassing of current through the target materials and the problem of charge accumulation, DC magnetron sputtering is unable to sputter low conducting and insulator materials. The use of RF magnetron sputtering can effectively overcome this constraint [2].

Tin oxide RF magnetron sputtering

The Sentaurus simulations relative to the fabrication process of tin oxide nanowires are based on experimental results found in literature. On table 3.5 the reference deposition conditions for tin oxide using RF magnetron sputtering are reported. This study was conducted to determine the optimized deposition conditions for obtaining SnO_2 films with the highest electrical conductivity, transmittance and thermoelectric power [8].

RF magnetron sputtering	Values
Source material	Sn target (99.999% purity)
Gas pressure	3-4x10^{-3} mbar
Ar gas flow	45.2 cm^3/min
O_2 gas flow	3.5 cm^3/min
Target-substrate distance	10 cm
RF power	15 W

Table 3.5. Deposition conditions for tin oxide RF magnetron sputtering.

3.3.2 Lift-off

Lift-off is a simple, straightforward approach for creating patterns on a substrate, particularly for noble metal thin films like platinum, tantalum, nickel, or iron, which are difficult to etch using traditional methods. The typical Lift-off procedure is as follows: photoresist is used to define a pattern on a substrate. A film, usually metallic, is deposited all over the substrate to cover the photoresist and regions where the photoresist has been removed. The photoresist beneath the film is dissolved with solvent during the actual lifting-off, taking the film with it and leaving only the film that was deposited directly on the substrate. On the following two different lift-off techniques are analyzed: single layer resist processing and bi-layer resist processing [21].

Single layer resist processing

Only one mask stage is required, as well as the conventional photolithography method. The primary disadvantage of this procedure is that the film is deposited on the photoresist sidewall (figure 3.8) and sticks to the substrate even after the resist has been removed (figure 3.9). This sidewall may be peeled off in subsequent processing [21].

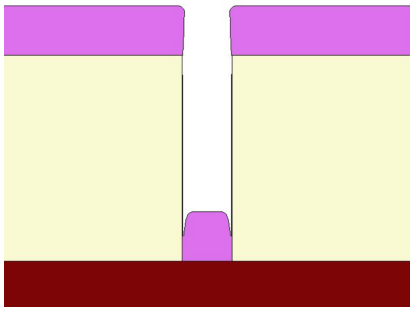

Figure 3.8. Single layer resist processing, before resist removal.

Immersion in acetone can be used to achieve lift-off. The time it takes for lift-off is determined by the film quality (the greater the film quality, the more impermeable it is and the longer it will take to lift off). A gentle swipe of a clean-room swab or a directed stream of acetone from a squeeze bottle can be used to remove the sidewalls from the film. The substrate must be kept immersed in acetone until all of the film has been removed and no traces of film particles can be found [21].

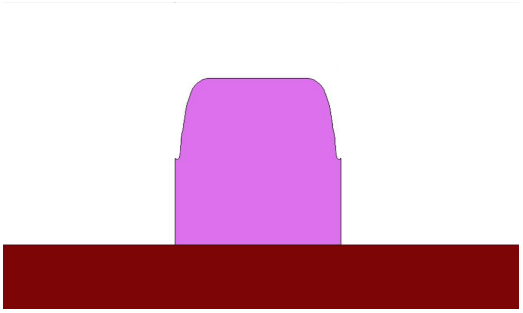

Figure 3.9. Single layer resist processing, after resist removal.

Bi-layer resist processing

This procedure necessitates the use of two layers of materials. First, a thin film of the assisting material is deposited. A layer of resist is spined over this layer and photolithographically patterned. This exposes the assisting material layer. The next step is to wet etch this layer so as to undercut the resist. The metal is subsequently deposited on the

wafer (figure 3.10), usually through a process called evaporation. The unwanted metal is removed along with the resist [21].

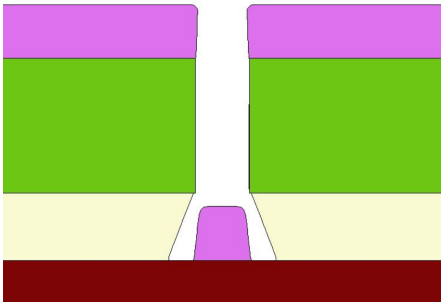

Figure 3.10. Bi-layer resist processing, before resist removal.

The assisting layer is then stripped off too, leaving only the metal pattern (figure 3.11) [21].

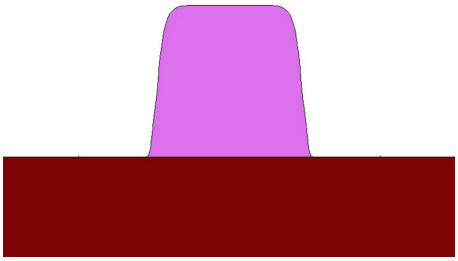

Figure 3.11. Bi-layer resist processing, after resist removal.

The disadvantages with respect to the single layer resist processing are: more complex to handle, more process steps. The advantages are: better resolution, no sidewall effect, regular window edge.

3.4 Tin(IV) oxide nanowires gas sensors

Many transition metal oxides show sensitivity to oxidizing and reducing gases by changing their electrical properties: variations in electrical conductance in response to environmental gases are typically monitored. For example, the conductivities of all of the following oxides indicate a gas response: Cr_2O_3, Mn_2O_3, Co_3O_4, NiO, CuO, CdO, MgO, SrO, In_2O_3, WO_3, TiO_2, V_2O_5, Fe_2O_3, GeO_2, $Nb2O_2$, MoO_3, Ta_2O_5, CeO_2 and ZnO. However, due to its suitable physicochemical features and lower cost compared to actual existing alternatives for similar applications, SnO_2 is currently the most extensively utilized material for detecting various gases. At moderate temperatures, it is sensitive to a variety of gases and

vapours, including ethanol, H_2, O_2, CO, NO, NO_2, and NH_2. Because surface chemical reactions are so important in gas sensing, there is a high correlation between gas sensitivity and surface chemical activities. Due to the easy adsorption of oxygen at its surface because of the intrinsic non-stoichiometry, SnO_2 has a strong reactivity to reduce gases at relatively low operating temperatures. Currently, the researches on this material are focused to increase its sensitivity, selectivity, stability and short response and recovery times [20].

3.4.1 Material properties

Rutile SnO_2 has tetragonal D_{4h}^{14} symmetry. It is a non-symmorphic crystal with two formula units per unit cell. Lattice parameters are a = 4.737 Å(a = b in the tetragonal structure) and c = 3.186 Å. Atomic positions are determined by the c/a ratio and the internal parameter u = 0.387. This crystalline structure contains metal atoms in octahedral coordination and oxygen in planar three-coordination. In SnO_2, chemical bonding is mainly governed by the linear combination of O 2s and 2p orbitals with Sn 5s and 5p orbitals. SnO_2 has a high chemical stability with respect to its chemical properties. The band gap is commonly quoted to be 3.6 eV at room temperature. Reduction of SnO2 surface converts the surface Sn cations from a (4+) to a (2+) valence state and creates the oxygen vacancies. Defect levels for oxygen vacancies lie just 114 meV below the conduction band minimum and thus can be easily thermally ionized. Table 3.6 summarizes the material properties of the SnO_2 [20].

Material properties	Values
Band gap	3.6 eV
a	4.737 Å
b	4.737 Å
c	3.186 Å
Volume	71.49Å^2
Hermann Mauguin	$P4_2/mnm$
Crystal System	Tetragonal

Table 3.6. Material properties of rutile SnO_2.

3.4.2 Substrates

The substrate selection is a crucial step when analyzing heteroepitaxial growth. On table 3.7 four different substrate materials are reported; for every substrate both the substrate and the film orientation are present as well as the corresponding minimal coincident interface area (MCIA) [11].
One value of minimal common unit cell area can be derived for each substrate and film pair. Films with different orientations that lie within the epitaxial geometrical limit are all feasible and will compete with one another under experimental conditions, whereas

the substrate and its orientation can be selectively chosen. To imitate this competition, we consider the growth orientation that yields the lowest minimal common unit cell area and hence the least incoherent interface, for any particular film. We can refer to the corresponding common unit cell area as the minimal coincident interface area (MCIA) and, by taking 40 integers of a typical unit surface cell, we can estimate a "small" MCIA criteria, e.g. $\leq 400\text{Å}^2$. We may assess the model on a set of substrate-SnO_2 pairs for which experimental results are available in the literature by using the two concepts of geometric surface area matching and film strain energy separately as selection criteria [5]. For this work silicon dioxide is used as a substrate since it is commercially viable and widely utilized in manufacturing and has a low value of minimal coincident interface area with respect to SnO_2.

Substrate material	Substrate orientation	Film orientation	MCIA [Å^2]
GaAs	<1 0 0>	<1 0 0>	133.9
SiO_2	<1 1 1>	<1 1 0>	151.5
GaN	<0 0 1>	<1 1 1>	185.6
AlN	<1 0 1>	<1 1 0>	189.4

Table 3.7. MCIA for different substrates.

Part II

Second Part

Chapter 4

Synopsys Sentaurus TCAD Suite

Technology Computer-Aided Design (TCAD) refers to the use of computer simulations to develop and optimize semiconductor process technologies and devices. Sentaurus is a suite of TCAD tools which simulates the fabrication, operation and reliability of semiconductor devices. The Sentaurus simulators use physical models to represent the wafer fabrication steps and device operation, thereby allowing the exploration and optimization of new semiconductor devices [13].
Process technology development is a difficulty for semiconductor companies due to time and cost restrictions. The number of engineering wafers required to complete the development of the new process is one important aspect that influences development time and cost. By simulating the process flow and device operation before any wafers are processed and during wafer-based process optimization, TCAD reduces the number of engineering wafers, saving time and money. Morever, Sentaurus TCAD simulations provide engineers with important insights on the behavior of semiconductor devices which can lead to new device concepts [13].
The use of Sentaurus TCAD leads to different benefits [13]:

- Improves device design, yield, and reliability by providing insight into advanced physical phenomena through self-consistent multidimensional modeling capabilities.
- With advanced structure generation, meshing, and numerics, it provides full-flow 3-D process and device simulation flows.
- Reduces technology development time and cost.
- With comprehensive physics-based processmodeling capabilities, it supports fast prototyping, development, and optimization of a wide range of semiconductor technologies.

The complete Sentaurus TCAD suite is schematically depicted in figure 4.1.

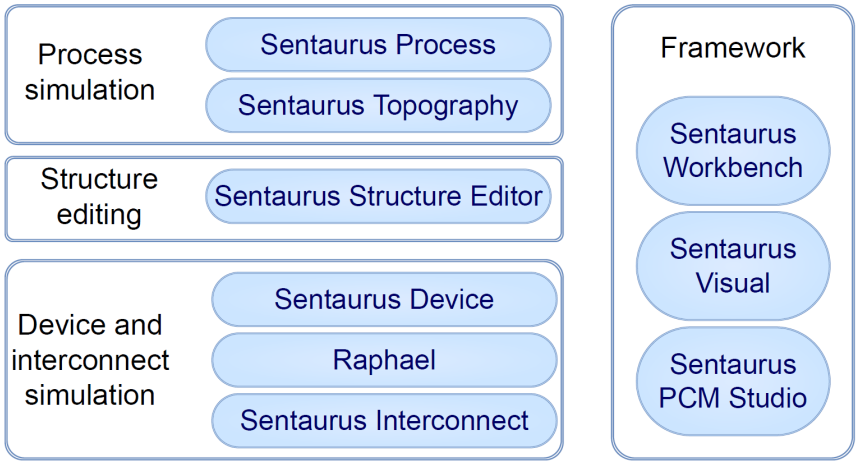

Figure 4.1. Sentaurus TCAD Suite.

Sentaurus TCAD is utilized to simulate the fabrication process steps and the electrical behaviour of the sensor device. Since Sentaurus TCAD is best suited to simulate lithographic techniques (such as mask-based deposition and etching) the top-down approach for the synthesis of SnO_2 nanowire sensors is simulated, consisting of sputtering of SnO_2 on the substrate and nanowire generation by lift-off of the photoresist. To generate the initial structure and define some material properties (such as the stiffness tensor for monocrystalline SnO_2 or the grain dimension for polycrystalline SnO_2) Sentaurus process is used while for advanced deposition techniques (plasma process that simulates RF magnetron sputtering) Sentaurus Topography is used. Finally, Sentaurus device is used for the electrical simulation.

4.1 Process simulation of single tin oxide nanowire device sensor

4.1.1 Sentaurus Topography 3D

The Synopsys Sentaurus^{TM} Topography 3D tool is a three-dimensional simulator for evaluating and optimizing critical topography-processing steps such as etching and deposition. Simple geometric etching and deposition techniques can be used to produce the initial structure, or TDR files can be read in. The structures that result can be saved in a variety of TDR file formats and used for further processing. Two simulation methods are used: the particle Monte Carlo (PMC) method and the level-set method. To the level-set method, which is the one used for this work, belong the following models [16]:

- Built-in models:
  - Deposition models: *crystal, electrodeposition, electroplating, hdp, hdp2, lpcvd, pecvd, pvd,* and *simple.*

  - Etching and simultaneous etching and deposition models: *crystal, dry, etchdepo, etchdepo2, hdp, ion_enhanced, ionmill, rie, rie2, simple,* and *wet.*

- Rate formula module (RFM)–based models (enables the definition of deposition and etching models using only built-in commands).

For the spin-on-glass deposition model (*spin_on*), the surface profile evolution is determined by solving a partial differential equation describing the motion of a fluid driven by evaporation, surface tension and centrifugal forces [16].
The processing time is divided into discrete time steps, and the exposed surface is discretized into a set of surface elements of finite extents when using the level-set method to simulate a model. The velocity at each surface element is determined based on the processing conditions at each time step, and the surface is updated. The velocity is calculated using the rate formula, which is unique to each model and describes mathematically the deposition or etching mechanisms relevant to the modeled process [16].
Sentaurus Topography 3D uses the idea of flux to simulate particle flow and interactions with the surface in level set–based models. A flux is an abstract continuum (statistical properties such as the angular distribution characterize a continuous flow) representation of one or more chemical species that play a similar role in the modeled process in this context. Every flux is characterized by its flux density, which describes the statistical distribution of the velocities of the particles as emitted from their source. The integrated flux density on a point on the surface is represented by the scalar quantity known as direct flux. The direct flux is the integral of the flux density over the visible range of a surface point, or the amount of particles per unit area and time that reach the surface before interacting with it. An indirect flux is a secondary flow that results from an interaction with the surface. As a result, according to the modeled physical effects, each flux has one direct flux and possibly several indirect fluxes. In the rate formula, all of these fluxes can be utilized. Sentaurus Topography 3D's computational flow can be represented as a loop over the following three steps when employing the level-set method [16]:

1. Compute the direct flux and all indirect fluxes for each flux at each surface point if the model relies on fluxes.

2. Using the rate formula, compute the velocity at each surface point.

3. According to the velocities provided by the rate formula, move the surface.

Modeling of fluxes

The reactant source (in most cases, a plasma) is assumed to be made up of two types of particles: neutrals and ions. Neutrals and ions are considered to be separate entities that do not interact. Furthermore, the pressure in the reaction chamber is thought to be very low for all plasma processes. As a result, ions and neutrals have a much longer mean free path length than the feature size. Fluxes are normalized in Sentaurus Topography 3D so that a flux integrated on an unshadowed flat surface is equal to one. Flux can be divided into two types [16].

Energy-independent fluxes with an isotropic angular distribution Electrically neutral species can be modelled using these fluxes. As a result, they are referred to as neutral fluxes. Neutrals are assumed to proceed in a straight path to the surface without colliding with other particles. Neutrals react with a particular probability on the surface, depositing or etching material. They are isotropically reemitted from the surface if they do not react. The reemitted particles can react with other particles or be reemitted. The reemitted particles can be reemitted again or can react elsewhere.

Energy-dependent and independent fluxes with an anisotropic angular distribution Charged particles can be modelled using these fluxes. As a result, they are referred to as ion fluxes. The assumption is that ions proceed in a straight path to the surface. Ions can react, be reflected, or sputter away surface material depending on the impinging angle on the surface. It is assumed that the ion is consumed during sputtering or reaction. The sputtered particles produce an indirect flux that can be redeposited on the surface. The sputtered particles can have an angular distribution with the symmetry axis either normal to the surface or in the direction of the reflected impacting ion, depending on the material being sputtered.

In figure 4.2 we can observe qualitatively the physical processes relevant to the process models based on the level-set method.

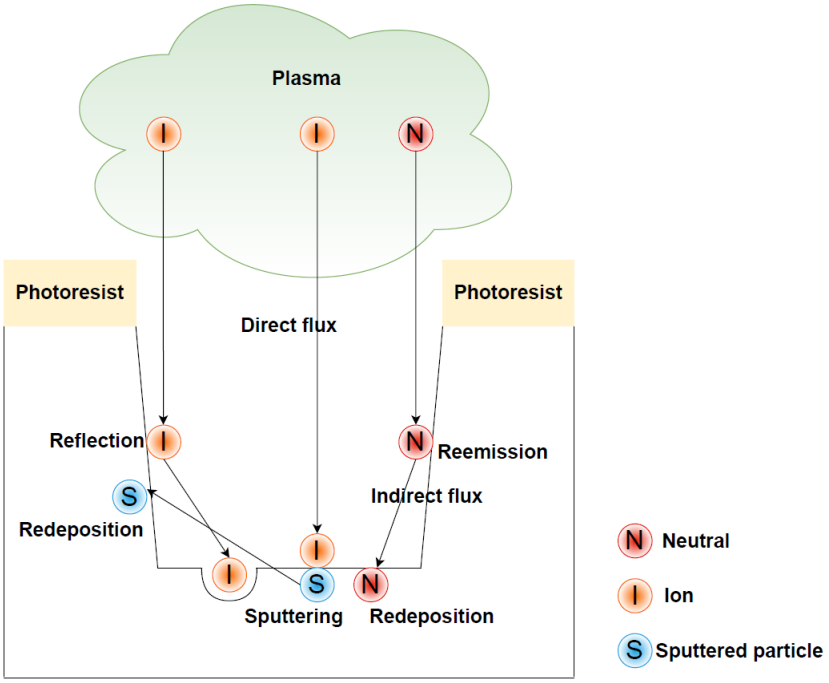

Figure 4.2. Overview of the physical processes relevant to the process models implemented in Sentaurus Topography 3D based on the level-set method.

Neutral flux

An isotropic source distribution, described as cos θ, characterizes a neutral flow. Neutral particles emitted from the source and arriving at a surface point j can react directly on the point j, or they can be reemitted from the surface multiple times and react at a surface point i.
The sticking coefficient is defiend as the reaction probability with the surface:

$$\sigma_{\mathrm{j}} = \frac{\Gamma_{\mathrm{reaction,j}}}{\Gamma_{\mathrm{neutral,j}}} = 1 - \frac{\Gamma_{\mathrm{re\text{-}emitted,j}}}{\Gamma_{\mathrm{neutral,j}}} \tag{4.1}$$

Where $\Gamma_{\mathrm{reaction,j}}$ is the fraction of the incoming flux that reacts, $\Gamma_{\mathrm{neutral,j}}$ is the total incoming neutral flux at surface element j and $\Gamma_{\mathrm{re\text{-}emitted,j}}$ is the fraction of the incoming flux that is reemitted. The sticking coefficient σ_{j} is not a constant in the whole surface. It depends on the material at the surface point j but not on the neutral species, and it varies between 0 and 1.
The sum of the direct neutral flux plus all contributions due to reemissions of the surrounding points j is the total neutral incoming flux on a surface point i:

$$\Gamma_{\mathrm{neutral,i}} = \Gamma_{\mathrm{direct,i}} + \sum_{j \neq i} (1 - \sigma_{\mathrm{j}}) g_{ij} \Gamma_{\mathrm{neutral,j}} \tag{4.2}$$

Where g_{ij} is the form factor that determines how much of the reemitted flux from the point j reaches the point i and $\Gamma_{\mathrm{direct,i}}$ is the direct flux arriving from the source at the point i.
The form factor depends on the reemission angular distribution and the surface geometry. Assuming that neutrals are reemitted with an isotropic angular distribution:

$$g_{ij} = \int_{A_j} \frac{cos\phi_i cos\phi_j}{\pi r_{ij}^2} V_{ij} dA_j \tag{4.3}$$

Where ϕ_i is the angle between the incoming particle direction and the surface normal, ϕ_j is the angle between the emitted particle direction and the normal of the surface of the emitter, V_{ij} is the mutual visibility matrix, dA_{j} is the area of the infinitesimal emitter and r_{ij} is the distance between the two surface elements i and j.

Ion flux

A directional angular source distribution characterizes the ion flux. The source distribution is either specified as an arbitrary ion-angular distribution function (IADF) using the command define_iad and the parameter iad in the corresponding etching or deposition models, or modeled as $\cos^{\mathrm{m}}\theta$, where the exponent m determines the flux anisotropy. To get a good approximation for measuring IADFs, the IADF can be defined analytically as:

$$f(\theta) = Acos^m(\theta) \tag{4.4}$$

Where A is a constant that is determined by normalizing the integrated ion flux on a flat unshadowed surface, θ is the angle between the vertical and the incoming ion direction and

m is a user-defined parameter (exponent) that describes the anisotropy of the distribution. The normalized flux is dimensionless as a result of flux normalization. As a consequence, multiplying the integrated and normalized flux on a surface element by the etching or deposition rate of a flat unshadowed surface yields the overall etching or deposition rate. The flux models of Sentaurus Topography 3D allow the definition of user-defined IADFs, which can have been obtained by measurement or from plasma simulations.
Some substrate material can be sputter by high-energy ions. The impact angle θ_{im} of the ions (the angle between the normal of the surface element and the incoming ion direction) has a big impact on the sputter etch rate. The yield function expresses this dependency:

$$\gamma(\theta_{im}) = s_1 cos\theta_{im} + s_2 cos^2\theta_{im} + s_4 cos^4\theta_{im} \tag{4.5}$$

where s_1, s_2, and s_4 are the sputtering coefficients. The sputtered flux is calculated in Sentaurus Topography 3D on the assumption of a narrow angular distribution (a large coefficient m in the angular distribution), for which the following formula can be written:

$$\Gamma_{\text{sputter,j}} = \gamma(\theta_{im})\Gamma_{\text{ion}} \tag{4.6}$$

where Γ_{ion} is the total direct ion flux, which is normalized. It is necessary that $\gamma(0) = 1$ for the sputtered flux Γ_{sputter} to be normalized so that the total sputtered flux from an unshadowed flat surface is unity. A relevant condition on the sputtering coefficients is achieved using this constraint:

$$s_1 + s_2 + s_4 = 1 \tag{4.7}$$

This means that just two parameters are needed to define the yield function $\gamma(\theta_{im})$, and Sentaurus Topography 3D utilizes the parameters s_1 and s_2.
Sputtered material can also be redeposited. The redeposition process is assumed to occur with probability $\sigma_{\text{redeposit}}$, and no further reemissions are considered, implying that the remaining $1 - \sigma_{\text{redeposit}}$ redeposit sputtered material is volatile. The flux of redeposition is:

$$\Gamma_{\text{redeposition,i}} = \sigma_{\text{redeposit}} \sum_{j \neq i} v_{ij} \Gamma_{\text{sputter,j}} \tag{4.8}$$

where v_{ij} is another form factor that accounts for how much of the sputtered material from the point j arrives at the point i:

$$v_{ij} = \int_{A_j} (m+1) \frac{cos\phi_i cos^m \phi_j}{\pi r_{ij}^2} V_{ij} dA_j \tag{4.9}$$

where ϕ_j now denotes the angle between the emitted particle direction and the symmetry axis of the sputtered material angular distribution.
There are differences between g_{ij} (defined for the neutral flux) and v_{ij}:

- v_{ij} is evaluated under some general assumptions. The angular distribution of the sputtered material, depending on the surface, can be either:

  - Diffuse: the sputtered particles have no memory of the impact direction, and the axis of the distribution is normal to the surface element.
  - Reflective: the sputtered particles keep some momentum of the impacting ion, and the axis of the distribution has a preferential direction, which is the reflected incoming ion direction.

- g_{ij} is evaluated under the assumptions that the reemission of neutrals can be approximated with an isotropic angular distribution. The symmetry axis of the angular distribution is the surface normal, and the exponent of the cosine distribution is one.

Low-energy ions with a large incident angle have a larger probability of being reflected by walls. This is an important phenomenon that contributes to microtrenching at the bottom of sidewalls. The probability that an ion is reflected is modeled according to:

$$P_{\text{reflection}}(\theta_{im}) = min\left\{1, k\left[\frac{1}{2\pi} + \left(\frac{\pi}{4} - \frac{1}{3}\right)\frac{1}{\left(\frac{\pi}{2} - \theta_{im}\right)^2} + \frac{5}{\pi^3}\left(\frac{\pi}{2} - \theta_{im}\right)\right]\right\} \tag{4.10}$$

where k is a constant that depends on the mass and atomic number of the incoming ion and the wall material, and on the ion energy:

$$k \propto \frac{1}{E_{ion}^2} \tag{4.11}$$

4.1.2 Sentaurus Process

The Synopsys Sentaurus Process tool is an advanced 1D, 2D, and 3D process simulator suitable for silicon and nonsilicon semiconductor devices. It features modern software architecture and state-of-the-art models to address current and future process technologies. Sentaurus Process simulates all standard process simulation steps, diffusion, analytic implantation, Monte Carlo implantation, oxidation, etching, deposition, and silicidation. Three-dimensional capabilities include meshing of 3D boundary files using the MGOALS module, mechanics (stress and strain), diffusion, a limited capability for 3D oxidation, and an interface to Sentaurus Structure Editor, which is the 3D geometry editing tool based on the ACIS solid modeling library [15].
Sentaurus Process provides an interface to Sentaurus Topography 3D, which is a three-dimensional physical etching and deposition simulator. The Sentaurus Topography 3D interface makes advanced etching and deposition models of Sentaurus Topography 3D available from within Sentaurus Process. The subset of 3D commands that are needed for etching and deposition is available through the interface. The topo command in Sentaurus Process enables all the interface functionality. The topo command is followed by the respective Sentaurus Topography 3D commands [15]:

```
topo {<Sentaurus Topography 3D commands>}
```

Listing 4.1. Sentaurus Topography 3D interface

Thanks to Sentaurus Process it has been possible to generate the initial structure, to simulate thermal oxidation od the silicon substrate to create the silicon dioxide layer, to define a polycrystalline stannic oxide and to compute mechanical stress.

Simulation settings

```
#Specifies the use of the unified coordinate system (UCS)
math coord.ucs

#Invokes the multithreaded operation
math numThreads= 8

#Allows the use of a set of parameters
AdvancedCalibration

pdbSet Grid MGoals Keep3DBrep 0
```

Listing 4.2. Beginning of the command file

The math coord.ucs command set the simulation coordinate system, the command specifies the use of the unified coordinate system (UCS). The visualization coordinates are identical to the simulation coordinates when using the UCS.
A set of models and parameters that have been calibrated to a broad range of technologies can be used with *AdvancedCalibration* in Sentaurus Process. Accurate results for many processes in device fabrication can be obtained with these parameters.
Some of the more advanced etching and deposition techniques (such as multimaterial etching, crystallographic etching and deposition, and Fourier etching and deposition) necessitate the use of the level-set method. This can take a long time, especially for 3D summations. MGOALS enables for a multithreaded solution of the level-set equations to reduce simulation time. The multithreaded operation can be triggered with the command: *math numThreads= 8*.

Initial structure generation

```
# Substrate definition

# x direction

line x location= 0<nm> spacing= 100.0<nm> tag= SiTop
line x location= 500.0<nm> spacing= 100.0<nm> tag= SiBottom

# y direction

line y location= 0.0 spacing= 100.0<nm> tag= Left
line y location= 4.25<um> spacing= 100.0<nm> tag= Right
```

```
# z direction

line z location= 0.0 spacing= 100.0<nm> tag= Back
line z location= 6<um> spacing= 100.0<nm> tag= Front

# Structure generation

region Silicon xlo= SiTop xhi= SiBottom ylo= Left yhi= Right
zlo= Back zhi= Front

init wafer.orient = { 1 1 1 } !DelayFullD

# Save the current structure
struct tdr= n@node@_NW1;

# Oxide deposition

deposit material= {Oxide} type= anisotropic time= 1<min>
rate= {0.5}

# Save the current structure
struct tdr= n@node@_NW2;
```

Listing 4.3. Initial structure definition and generation

In most simulations, the first step is to load an existing structure or generate a new one. A combination of the *line*, *region*, and *init* commands is used to create new structures. The initial mesh is a tensor-product mesh where the density of lines is specified using the *line* command, and the regions are defined by specifying tags in the *line* commands and defined in the *region* command. The initial regions are always defined as three-dimensional axis-aligned bricks. The structure is defined by combining the *line* and *region* commands. The structure is actually formed in the *init* command. Thus, the command: *line x location= 0<nm> spacing= 100.0<nm> tag= SiTop* means that we are creating a mesh with a size of 100 nm starting from the top of the substrate. In particular, the argument spacing defines the spacing between two grid lines at the specified location. Notice that units in Sentaurus can be specified explicitly by giving the units in angle brackets. For most cases, the default unit of length is micrometer. The coordinate 0.0 of the substrate is named SiTop using the tag=statement for later use in the region command. The same is valid for the y axis and the z axis. It is important to remark that, while for the x axis and z axis the dimensions are the actual structure dimensions, for the y axis only half structure is generated. This strategy is used to reduce the simulation time, thus, only half of the structure was created and later the structure was mirrored creating the complete device. The command *region Silicon xlo= SiTop xhi= SiBottom ylo= Left yhi= Right zlo= Back zhi= Front* identifies a region made of Silicon, defined by the coordinates xlo, xhi, ylo, yhi, zlo, zhi.
The *init wafer.orient = { 1 1 1 }* command specifies the principal wafer orientation,

where {1 1 1} specifies the crystallographic (Miller) indices for the wafer orientation plane (according to what is on section 3.4.2).

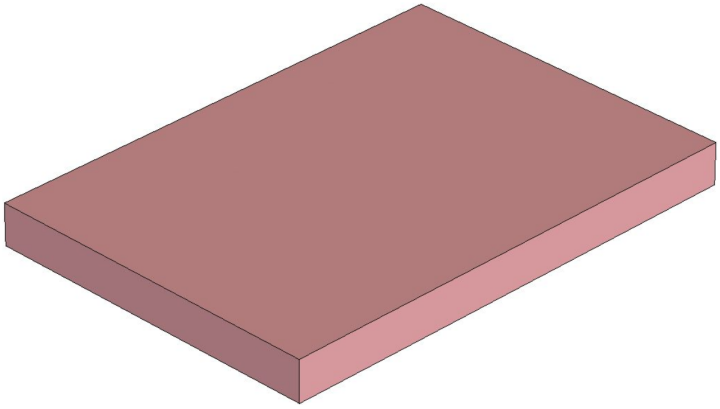

Figure 4.3. Silicon substrate.

Sentaurus Process automatically extrudes the structure and mesh into the appropriate dimension and copies the data when a 2D or 3D mask is used in an etch, deposit, or photo command. The option *!DelayFullD* can be used in the init command to disable the full-dimensional structure creation delay.

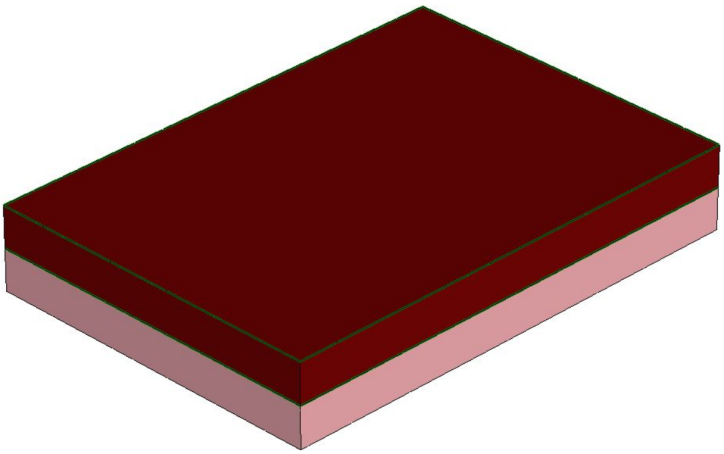

Figure 4.4. Si/SiO_2 substrate.

The command *struct tdr= n@node@_NW1;* is used to save the current structure to see the intermediate steps of the process (figure 4.3).
The command *deposit material= Oxide type= anisotropic time= 1<min> rate= 0.5* is used to perform an anisotropic (growth only in the vertical direction) deposition of 500 nm of SiO_2 (figure 4.4).

On table 4.1 the device parameters used in the simulations are reported; note that some of them are not present in the command file but in the parameter files.

Parameter	Value
Tin oxide bandgap	3.6 eV
Permittivity of SnO_2 nanowire	13.50
Permittivity of silicon oxide	3.9
Electron mobility	9.33 x 10^{-4} $\frac{m^2}{Vs}$
Donor density	9.146 x 10^{24} m^{-3}
Nanowire diameter	120 x 10^{-9} m
Channel length	7 x 10^{-6} m
Channel width	120 x 10^{-9} m
Oxide thickness	500 x 10^{-9} m

Table 4.1. Device parameters.

Spin-on-glass deposition

```
#Spin-on-glass
topo define_deposit_machine model=spin_on material=Photoresist \
viscosity=0.015 density=1 initial_thickness=0.55 \
radial_distance=2e4 surface_tension=27 angular_velocity=4000 \
evaporation_rate=0 angular_position=0

#Deposition
#Courant Friedrichs Lewy (CFL) number for the integration of
the surface evolution equation.
topo deposit spacing={0.3 0.3} time=0.01 cfl=0.025

# Save the current structure
struct tdr= n@node@_NW3;
```

Listing 4.4. Spin-on-glass deposition

To determine the spin-on photoresist profile over a particular topographic substrate, the spin_on model is utilized. The film profile evolution is calculated by solving the Navier Stokes equations under the lubrication theory for Newtonian fluids. The profile evolution of the film is determined using the initial thickness of the spin-on material (parameter initial_thickness) and the capillarity and centrifugal forces acting on it. In addition, the film is supposed to evaporate (parameter evaporation_rate) during the process. The viscosity (parameter viscosity), density (parameter density), and surface tension with the surrounding fluid (parameter surface_tension) characterize the spin-on material. The centrifugal force acting on the simulated structure is determined by the angular velocity of the wafer (parameter angular_velocity), the position of the simulated structure on the

wafer (parameters angular_position and radial_distance), and the film density and it is supposed to be constant over the simulation domain.
Since the spin on technique is typically used to deposit the photoresist on the substrate, the spin-on-glass deposition method is used for the deposition of the photoresist (figure 4.5). Note that, since the vertical dimension does not need to be discretized, for the spin-on-glass deposition model only the spatial discretizations along dimensions orthogonal to the vertical can be set, thus, only two dimensions are set for the spacing parameter.

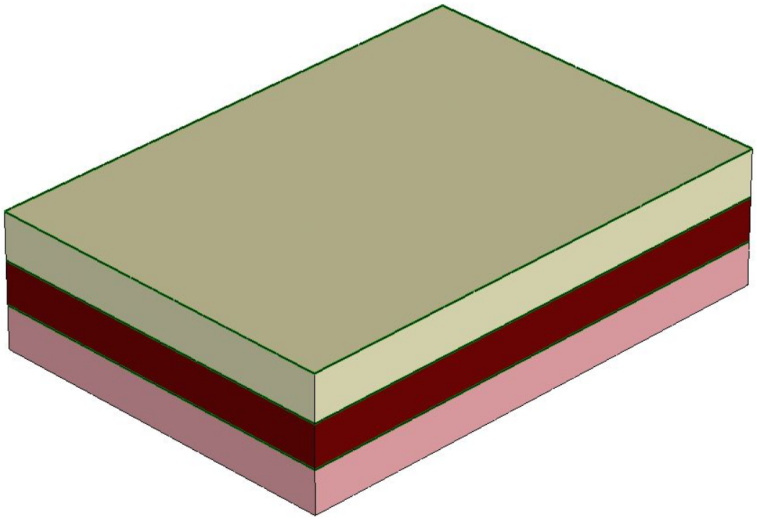

Figure 4.5. Photoresist after spin-on-glass deposition.

Etching of photoresist

```
# Read geometry, data, and PDB parameters from n1_NW3_fps.tdr

init tdr= n1_NW3_fps

# Mask definition
mask name=nanowire_mask left= 0.0<um> right= 3.75<um>
back=2.94<um> front=3.06<um> negative

# Photoresist etch
etch material= {Photoresist} type= anisotropic time= 1
rate= {0.7} \
     mask= nanowire_mask

# Save the current structure
struct tdr= n@node@_NW4;
```

Listing 4.5. First photolithographic step

The fabrication process of the nanowire sensor has been splitter in more simulation, mainly because of better work organization and shorter simulation times.
On the second command file (second simulation) the first photolithographic step and the physical vapor deposition of SnO_2 are performed.
To go from one simulation to the other, the init command can be used at the beginning of the file to read the structure from the previous file. The command *init tdr= n1_NW4_fps* is used to read the structure; thus, for every simulation the initial structure is the final structure of the previous simulation, and the final structure will be the initial structure of the following simulation. In this case the initial structure is the one on figure 4.5.
Next the nanowire pattern must be made on the photoresist (since a lift-off technique is used) through a lithography process. To this end, a mask must be firstly defined with the following command: *mask name=nanowire_mask left= 0.0<um> right= 3.75<um> back=2.94<um> front=3.06<um> negative*. If negative command is used, the points outside the defined region are considered masked; if positive or no command is used, the points inside the defined region are considered masked.
Now the photoresist is etched. Since a negative mask is declared, only the area covered by the mask is etched. The etching depth is bigger than the thickness of the photoresist layer, thus no residual material remains. The etching type is anisotropic, in this case it means that there will be no undercuts (figure 4.6).

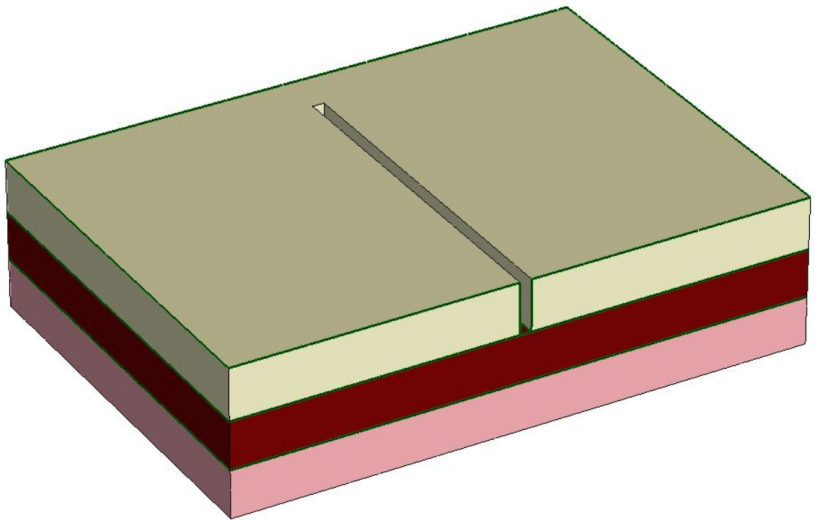

Figure 4.6. Etched photoresist.

Polycrystalline SnO_2

```
#Tin oxide is created and made to be like polycrystalline silicon
mater add name= SnO2 new.like= PolySilicon
```

```
#Specify crystal orientation
mater name= SnO2 vertical.orient= {1 0 0}

#set the crystallinity to polycrystalline
pdbSet SnO2 Crystallinity Polycrystalline

#Switch on growth model
pdbSet SnO2 Dopant DiffModel Granular

#Set in the parameter database the grain shape and the initial
values for the grain size L and grain boundary thickness
pdbSet SnO2 GrainShape Cubic
pdbSet SnO2 GrainSize 5.0e-6
pdbSet SnO2 GrainBoundaryThickness 5.0e-8

#Set the layer thickness
pdbSet SnO2 LayerThickness 1.0e-6

#Reset the grain size dataset GSize to the current value of
GrainSize
pdbSet SnO2 GbcNew 1
```

Listing 4.6. Polycrystalline tin oxide

Using the special *like* parameter in the Parameter Database (PDB), a material's parameters can be inherited from the parameters of another material. The two materials are referred to as like materials when this is the case. Different settings in different regions can be specified using this method. To begin, a new material is generated and made to be like an existing material using the command *mater add name= SnO2 new.like= PolySilicon*; where *name* specifies the name of the material to be created and *new.like* is the name of the existing material from which all default values are inherited. The polysilicon has a semiconducting behavior just like the tin oxide and, moreover, for polysilicon the parameter *Crystallinity* is available in the PDB.
One way to change the crystallinity (*Amorphous*, *Crystalline*, and *Polycrystalline*) of a material is to use the parameter *Crystallinity* to set the crystallinity: *pdbSet SnO2 Crystallinity Polycrystalline*.
A polycrystalline material is characterized by its crystal orientation and grain size. Crystal orientation (one of <100>, <110>, and <111>) can be specified using the material-specific command *mater name= SnO2 vertical.orient= {1 0 0}* (the nanowires are grown in [100] direction).
The model does not include information about the microscopic shape and size of the grains. Instead, all parameters that are dependent on grain size are computed using the size, orientation, and type of a prototype grain. The growth model can be switched on by the command: *pdbSet SnO2 Dopant DiffModel Granular*. Sentaurus Process assumes a columnar grain structure by default. The grains are assumed to be columns that are oriented along the vertical axis, extending through the entire polycrystalline layer. The

grain size L defines the average edge length of the square cross section of the columns. The grain size is stored in the dataset *GSize*. Columnar grains and cubic grains are schematically depicted in figure 4.7, where L is the grain size, δ is the grain boundary thickness, and d is the layer thickness.

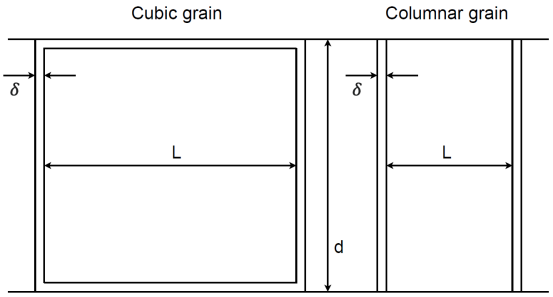

Figure 4.7. Cubic grains (left) and columnar grains (right).

The volume share of the grain region is given as:

$$f_g = \left(\frac{L}{L+\delta}\right)^2 \tag{4.12}$$

The volume share for cubic grains is:

$$f_g = \left(\frac{L}{L+\delta}\right)^3 \tag{4.13}$$

The initial values for the grain size L (cm) and grain boundary thickness δ (cm) and the grain shape can be set in the parameter database by the commands *pdbSet SnO2 GrainShape Cubic*, *pdbSet SnO2 GrainSize 5.0e-6* and *pdbSet SnO2 GrainBoundaryThickness 5.0e-8*. The layer thickness d is assumed to be a constant value set by: *pdbSet SnO2 LayerThickness 1.0e-6*. Thermal processes cause the grains to grow. The volume share of grains increases as grain growth progresses, whereas the volume share of the grain boundary decreases. The following equation is used to model grain growth:

$$\frac{dL}{dt}L = \frac{\tau^2 a_0 b_0^2 D\lambda}{kT}\frac{1}{1+\frac{1}{a_r}}\left(1-\frac{\sum c_{gb}}{C_{Si}}\right) \tag{4.14}$$

where a_r denotes the ratio between the grain boundary volume inside the polycrystalline layer and the grain boundary volume at the material interfaces of the polycrystalline layer bounding other materials. The grain size, L, is represented with the solution name *GSize* and can be monitored in the same way that other solution fields can be. The grain growth parameters can be defined in the parameter database in the material entry. τ *Tau*, λ *Lambda* and a_0 *A0* are the names that are utilized. The parameter b_0 is equal to twice the lattice spacing of silicon. The Arrhenius values for the various contributions to the self-diffusivity D can be specified with the parameter *Dself*. For columnar grains:

$$a_r = \frac{(2L+\delta)d}{2(L+\delta)^2} \tag{4.15}$$

$$\frac{dL}{dt}L\left(1+\frac{2(L+\delta)^2}{(2L+\delta)d}\right) = \frac{\tau^2 a_0 b_0^2 D\lambda}{kT}\left(1-\frac{\sum c_{gb}}{C_{Si}}\right) \tag{4.16}$$

For cubic grains:

$$a_r = \frac{(3L^2+3L\delta+\delta^2)d}{2(L+\delta)^3} - \frac{1}{2} \tag{4.17}$$

$$\frac{dL}{dt}L\frac{d(3L^2+3L\delta+\delta^2)+(L+\delta)^3}{d(3L^2+3L\delta+\delta^2)-(L+\delta)^3} = \frac{\tau^2 a_0 b_0^2 D\lambda}{kT}\left(1-\frac{\sum c_{gb}}{C_{Si}}\right) \tag{4.18}$$

When the grain size L reaches the layer thickness d and the grain shape is set to *Cubic* the grain shape switches from *Cubic* to *Columnar*. if the grain shape is set to *Columnar* no switching is performed. The grain growth equation is solved with the dopant diffusion equations. At the beginning of a new diffusion step the *GSize* and the dopant distribution in the grain boundary *<dopant>Gbc* are not reset automatically. To reset the grain size dataset *GSize* to the current value of *GrainSize* the pdb switch *GbcNew* can be used: *pdbSet SnO2 GbcNew 1*.

Physical vapor deposition

```
#PVD
topo define_deposit_machine material=SnO2 model=pvd rate=1.1 \
exponent=10000

#Deposition
topo deposit spacing={0.01 0.01 0.01} time=0.15

# Save the current structure
struct tdr= n@node@_NW5;
```

Listing 4.7. Physical vapor deposition

The PVD model is applicable to deposition processes that include just physical processes rather than chemical interactions. A $\cos^{\mathrm{m}}\theta$ angular distribution characterizes the particle flux, where m is determined by the exponent parameter (as in this case) or a user defined IADF (the iad parameter). Each incoming particle deposits on the surface because the sticking coefficient is one. The rate parameter is used to set the deposition rate R_0 on an unshadowed flat surface. The total deposition rate is calculated as:

$$R = R_0\Gamma \tag{4.19}$$

Where Γ is the integrated flux on the considered surface point.
The deposition process on which the simulations are based is RF magnetron sputtering of polycrystalline SnO_2 (section 3.3.1), thus, being the sputtering a physical vapor

deposition, the best deposition model in this case is the pvd model provided by Sentaurus Topography 3D (figure 4.8). For these three-dimensional simulations for evaluating and optimizing critical topography-processing steps such as physical vapor deposition, the required memory and CPU time are determined mainly by the spatial and time discretization. This led to two trade-offs during the simulations:

- Minimum grid spacing of dx=10nm, dy=10nm and dz=10nm, due to the fact that lower values cause the simulation to fail. Lower spacing values provide better results, but this was not possible due to simulation failure.

- Maximum exponent of 10000, due to the fact that higher values cause the simulation to fail. Higher exponent values provide better results (the deposition becomes more anisotropic), but this was not possible due to simulation failure.

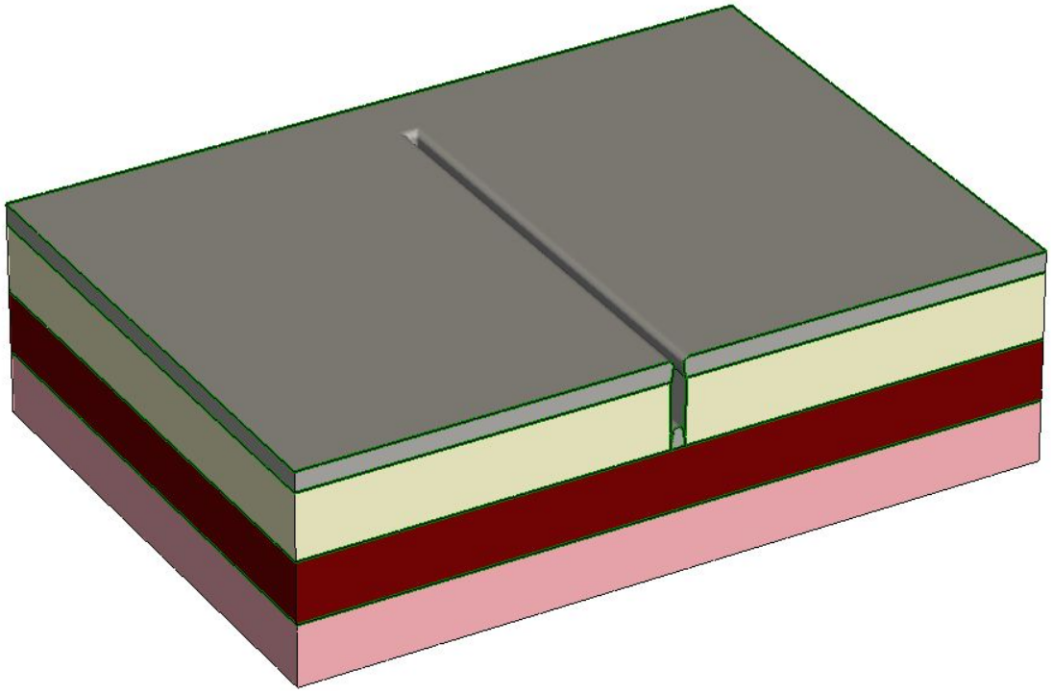

Figure 4.8. SnO_2 physical vapor deposition.

On figure 4.9 a cross-section view of the structure after the physical vapor deposition is present. A single layer resist lift-off process was simulated since Sentaurus was not able to simulate a bi-layer resist lift-off process using Topography 3D. On the sidewalls of the photoresist a very thin layer (less than 1 nm) of SnO_2 is present; however, after having verified with Topography 2D that this thin SnO_2 film is not present in a realistic situation, it has been removed before the photoresist removal.

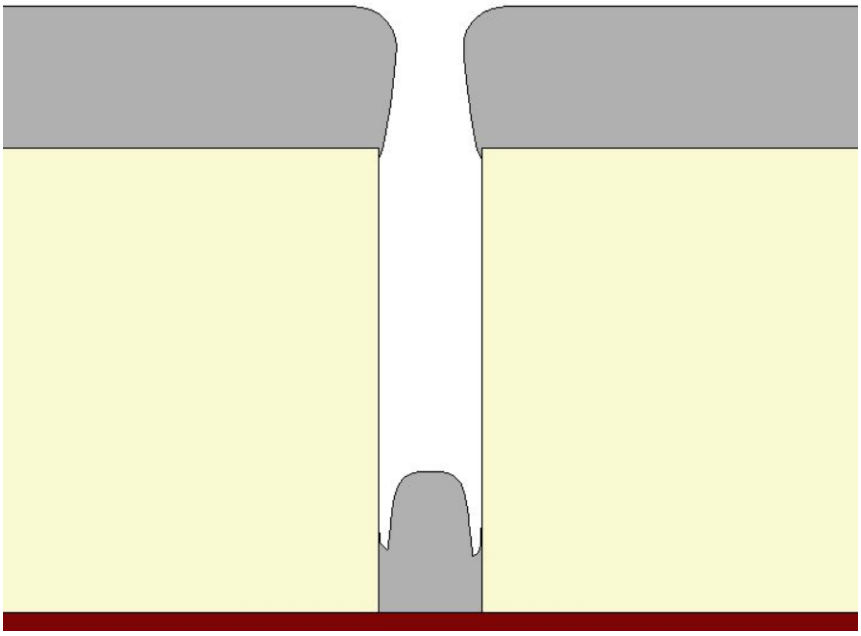

Figure 4.9. SnO_2 physical vapor deposition cross-section view.

After the photoresist removal only the tin oxide nanowire is left as we can see on figure 4.10 (the silicon substrate in pink, the silicon dioxide in vinaceous and the tin oxide nanowire in silver).

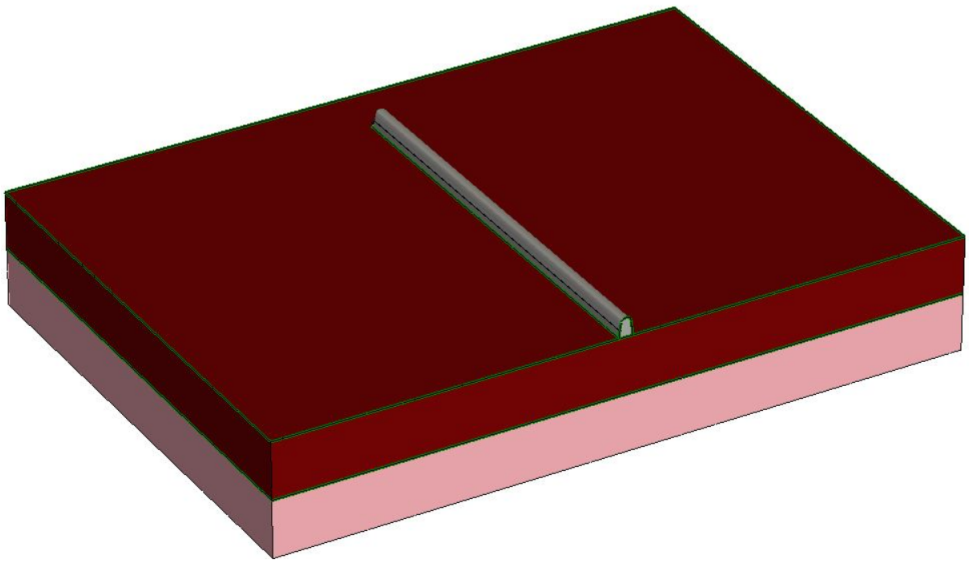

Figure 4.10. SnO_2 nanowire after resist removal.

On figure 4.11 a cross-section view of the structure after photoresist removal is present. As discussed previously on section 3.3.2, with the single layer lift-off procedure an irregular nanowire geometry near the photoresist sidewall is obtained.

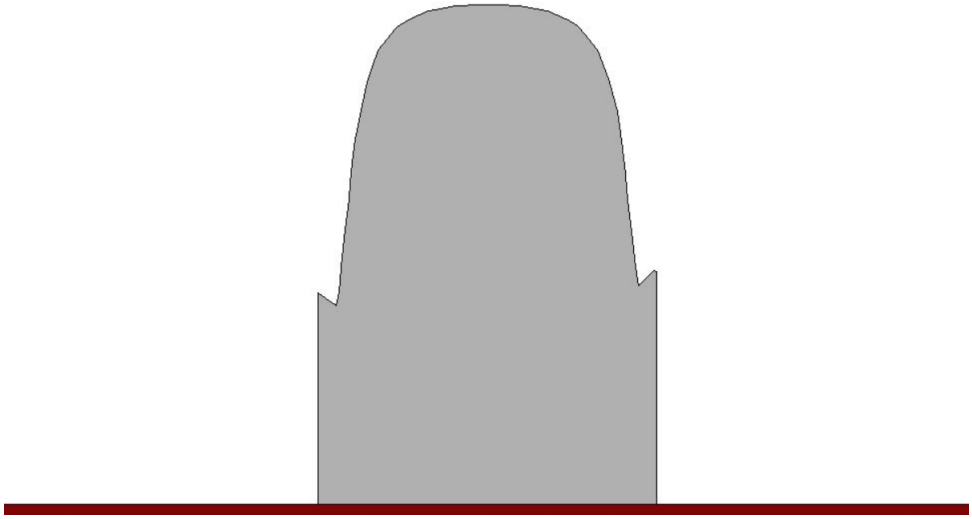

Figure 4.11. Cross-section view of SnO_2 nanowire after resist removal.

Contacs

```
# Mask creation

polygon name= ContactShape segments= {4 4.5 4 5.7 3 5.7 3 4.5
3.26 3.56 3.26 2.69 3.62 2.69 3.62 3.56}
mask name= contactmask polygons= {ContactShape}

# Contact deposition

deposit material= {Titanium} type= isotropic time= 1<min>
rate= {0.01}
struct tdr= n@node@_NW6;
deposit material= {Gold} type= isotropic time= 1<min>
rate= {0.1}
struct tdr= n@node@_NW7;

# Photoresist deposition

deposit material= {Photoresist} type= anisotropic time= 1<min>
rate= {0.5}
```

```
struct tdr= n@node@_NW8;

# Photoresist etch

etch material= {Photoresist} type= anisotropic time=1 rate={1} \
     mask= contactmask

struct tdr= n@node@_NW9;

# Contact etch

etch material= {Gold} type= anisotropic time= 1 rate= {1}
etch material= {Titanium} type= anisotropic time= 1 rate= {0.5}

struct tdr= n@node@_NW10;

# Photoresist removal

strip Photoresist

struct tdr= n@node@_NW11;
```

Listing 4.8. Contact definition and deposition

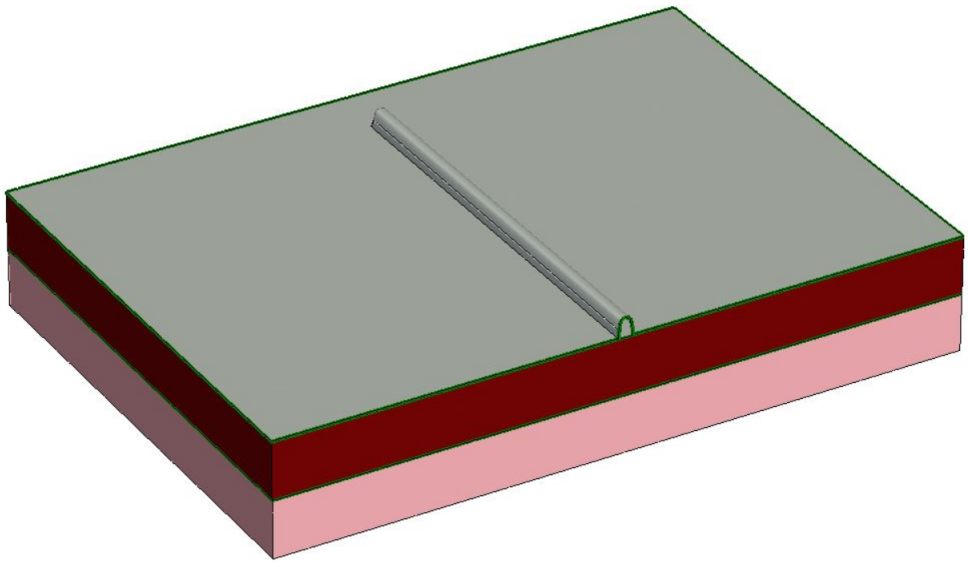

Figure 4.12. Titanium deposition.

First, a positive contact mask is created using the polygon command. The command *polygon name= ContactShape segments= {4 4.5 4 5.7 3 5.7 3 4.5 3.5 3.56 3.51 2.69 3.61*

2.69 3.62 3.56} defines a polygon given as {x1 y1 x2 y2 ... xn yn}. Note that this is a positive mask since the contact are not created using the lift-off technique just like the nanowire.
The contacts are deposited; Ti/Au (10nm/100nm) contacts are used. First the titanium is deposited ((figure 4.12)), then the gold is deposited ((figure 4.13)).

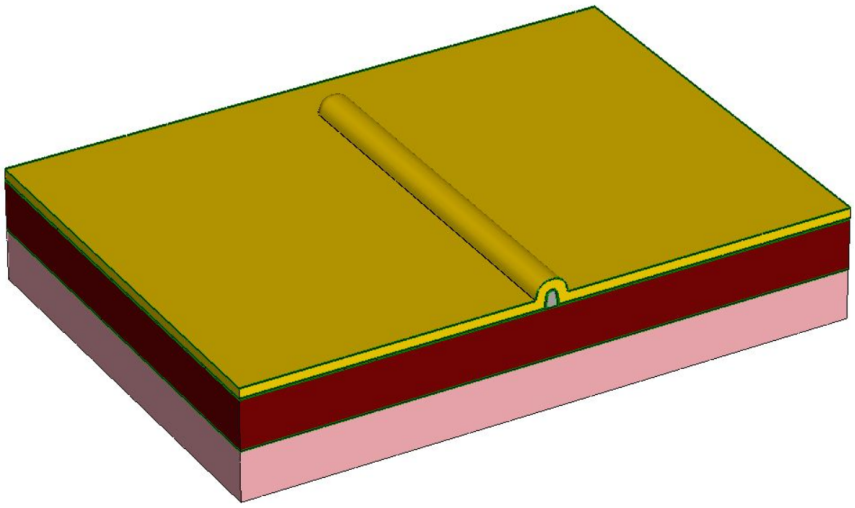

Figure 4.13. Gold deposition.

Thus, the photoresist is deposited (figure 4.14).

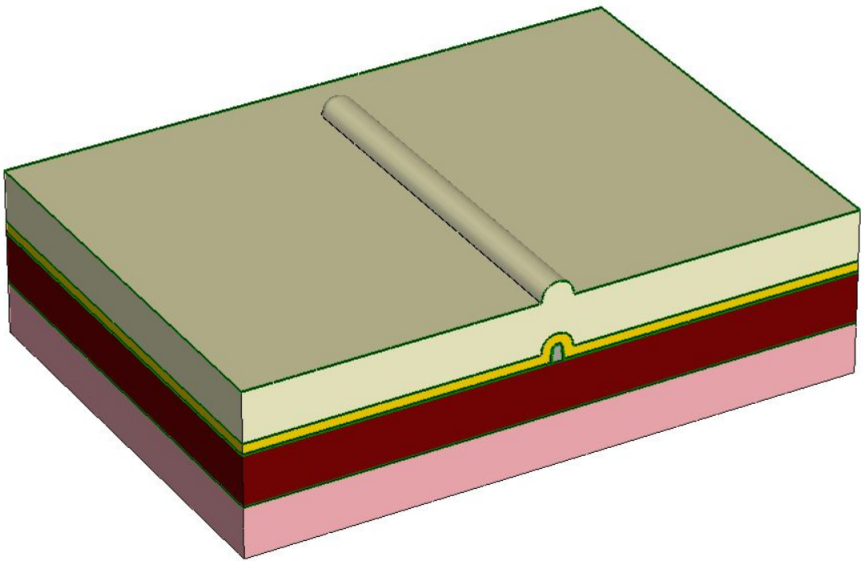

Figure 4.14. Photoresist deposition.

The photoresist is then etched using the contact mask previously defined (figure 4.15).

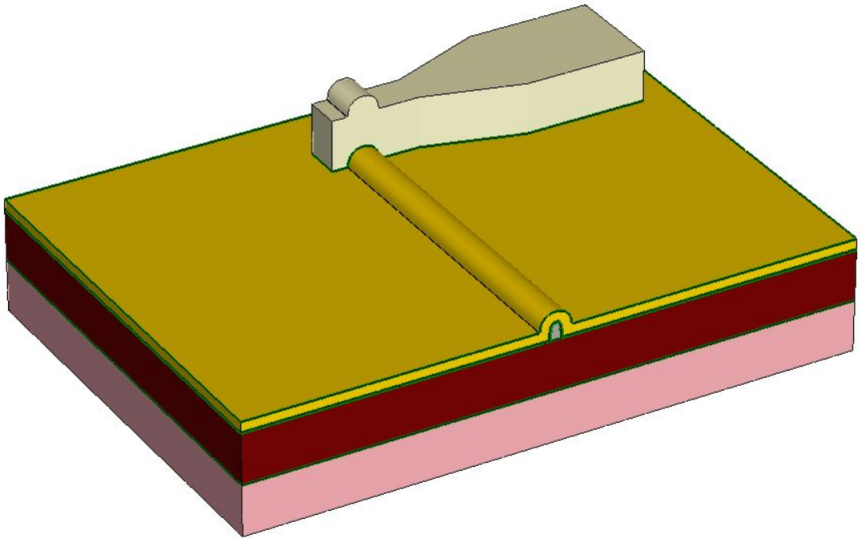

Figure 4.15. Photoresist etching.

The titanium and the gold are etched anisotropically and only the metals under the photoresist are left (figure 4.16).

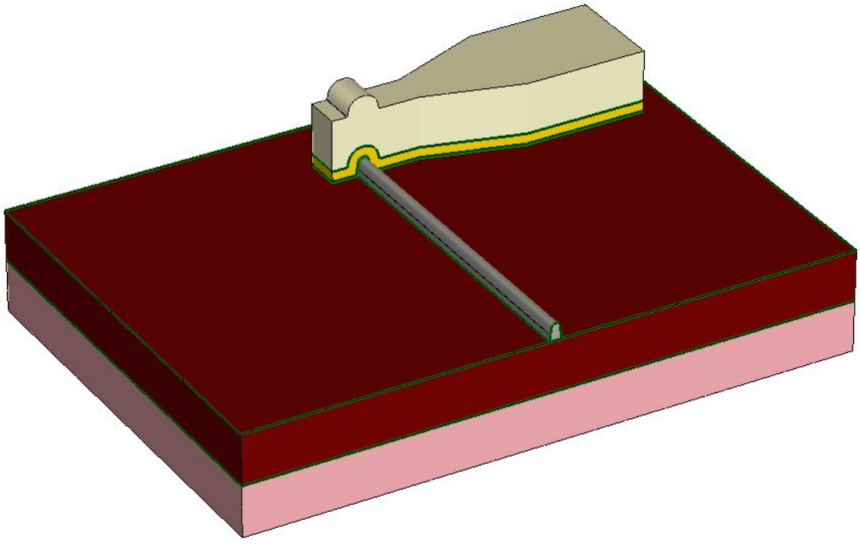

Figure 4.16. Contacts etching.

Finally, the photoresist is removed (figure 4.17).

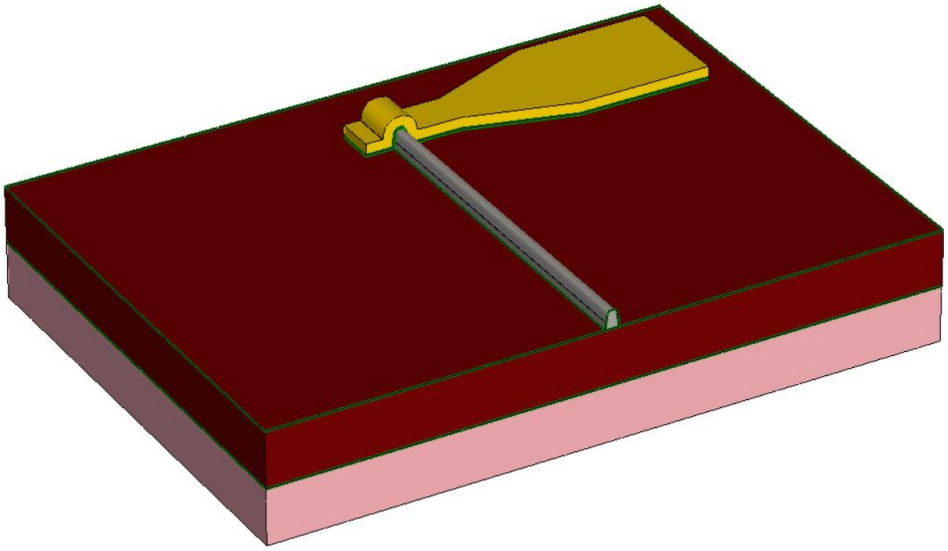

Figure 4.17. Photoresist removal.

Contact pad and structure mirroring

```
# Contact pad deposition

deposit material= {Aluminum} type= fill coord= -0.82

etch material= {Aluminum} type= anisotropic time= 1 rate= {1} \
     mask= contactmask

struct tdr= n@node@_NW12;

# Structure mirroring

transform reflect left

struct tdr= n@node@_NW13;
```

Listing 4.9. Contact pad deposition and mirroring

For a point contact (like in this work), we specify a point inside a chosen region. The chosen region is removed, and all interfaces between the chosen region and bulk materials become part of the contact. To consider the physical properties of the contacts and their interactions with the nanowire, for a situation as realistic as possible, aluminum pads are deposited above the contacts (figure 4.18). The material in this case has no importance since Sentaurus will remove the aluminum and will change it with the Gas.par material. In this way during the electrical simulation the contacts are considered.

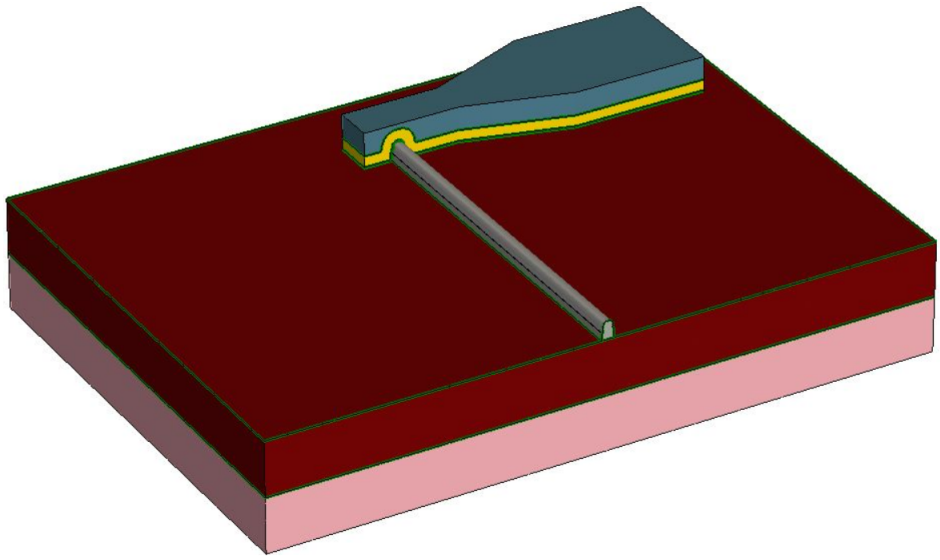

Figure 4.18. Contact pad.

Now the structure is mirrored creating the complete device (figure 4.19).

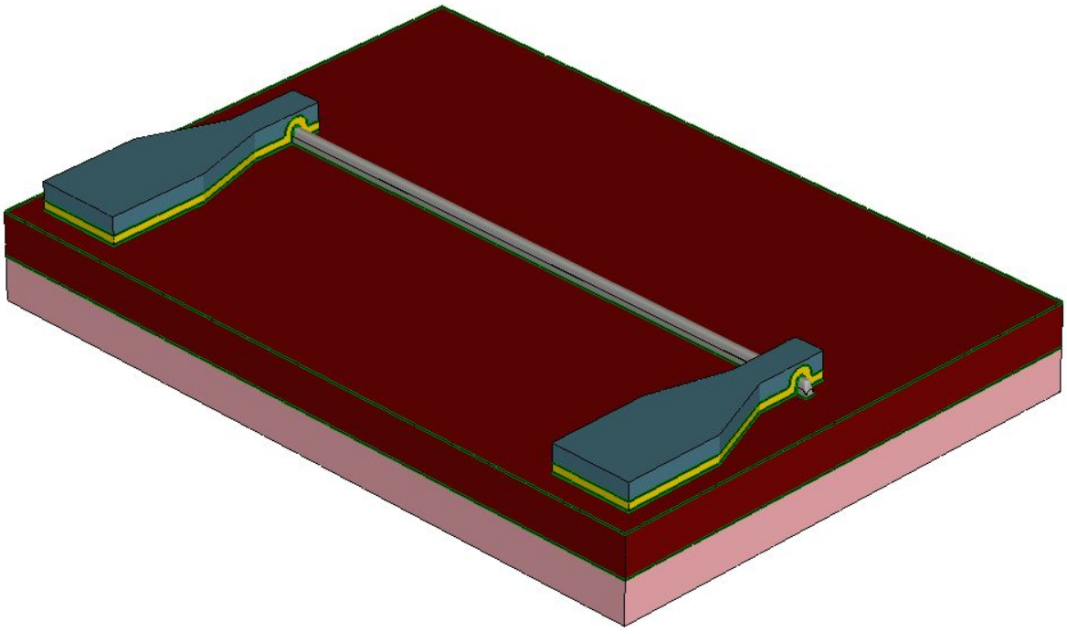

Figure 4.19. Mirrored structure.

The transform *reflect left* command is used to perform the reflection centered on the

outer boundary of the simulation domain. At the reflection side, regions are not merged immediately to allow a clean transform cut afterwards if required.

Remesh and contact defnition

```
init tdr= contact_fps

# Clear the process mesh

refinebox clear
line clear

# Reset default settings for adaptive meshing

pdbSet Grid AdaptiveField Refine.Abs.Error 1.e37
pdbSet Grid AdaptiveField Refine.Rel.Error 1e10
# pdbSet Grid AdaptiveField Refine.Target 500.0

# Specify adaptive refinement

pdbSet Grid Adaptive 1

mgoals accuracy= 1e-5

# Set mesh spacing near interfaces

pdbSet Grid SnMesh min.normal.size 0.01
# pdbSet Grid SnMesh normal.growth.ratio.2d <n>
pdbSet Grid SnMesh normal.growth.ratio.3d 8.0

# Set high-quality Delaunay meshes

pdbSet Grid SnMesh DelaunayType boxmethod

# Set which interfaces will have interface refinement

refinebox interface.materials= {SnO2}
refinebox interface.materials= {Oxide}
refinebox interface.materials= {Gold}
refinebox interface.materials= {Titanium}

# Specify refinement boxe

refinebox min= {-0.668 -3.748 2.9438} max= {-0.495 3.748 3.0565}
xrefine= 5<nm> yrefine= 5<nm> zrefine= 5<nm>
```

```
grid remesh

contact name = source x= -0.7 y= -3.4 z= 4 Aluminum

contact name = drain x= -0.7 y= 3.4 z= 4 Aluminum

struct tdr= final;

exit
```

Listing 4.10. Contact pad deposition and mirroring

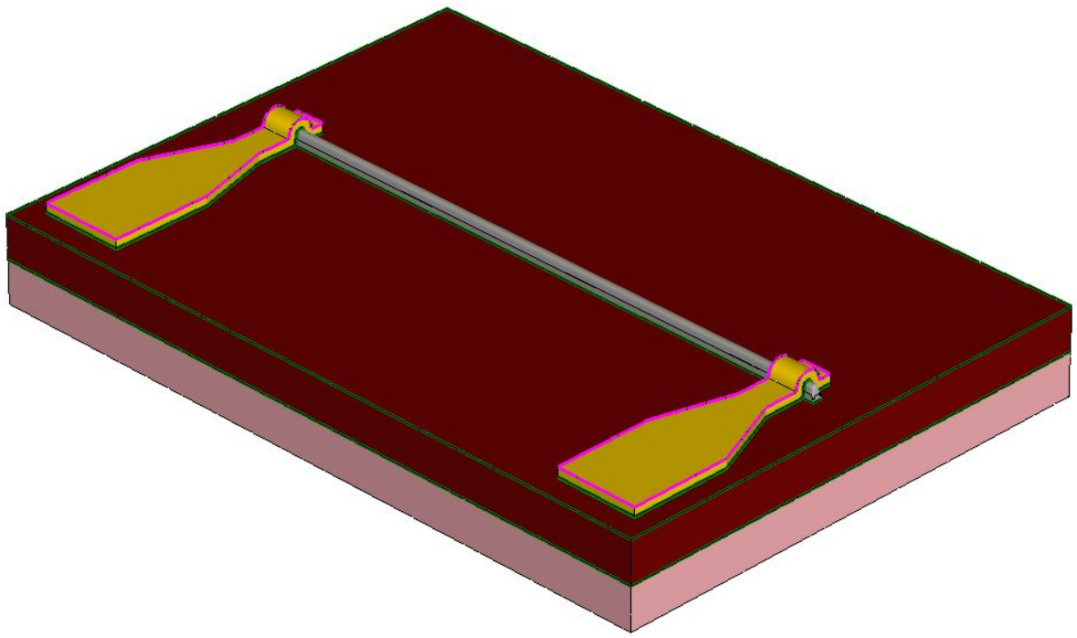

Figure 4.20. Final structure.

Mechanical stress

This section, related to the mechanical stress, is separate from the rest of work since polycrystalline SnO_2 has been chosen over monocrystalline SnO_2, thus, there is no need to simulate stress.
In process modeling, mechanical stress plays a significant role. Mechanical stress controls the structural integrity of the device, the yield from the process depends on stresses, the mobility of charged carriers is affected by stresses, and leakage currents also are a function of the stress in the system. Stresses can affect dopant diffusion rates on a finer scale by changing the band gap. They can alter the shapes of thermally grown oxide layers

by affecting oxidation rates. Stress computation accuracy is critical in modern process flows. However, there is a growing tendency toward designing process flows that generate the appropriate types of stress in the device. Device performance can be considerably improved with the appropriate stresses. Stress computation simulations are carried out in four distinct steps:

1. Define the mechanics equations. The equations used in Sentaurus Process define force equilibrium in the quasistatic regime.

2. For these equations, define the boundary conditions. Provided that certain criteria are met, Sentaurus Process allows Dirichlet or Neumann boundary conditions.

3. Define the properties of the material. The relationship between stresses and strains is defined in this step. Elastic materials are those that can hold stresses for a given strain without relaxing. Other materials, such as viscous or viscoelastic materials, can relax the stresses away. For the computation of mechanical stresses, Sentaurus Process provides viscoelastic constitutive equations. The Maxwell model and the standard linear solid model are both available in the viscoelastic models utilized in Sentaurus Process. The viscosity can be affected by local shear stresses, making it a locally variable quantity that can cause nonlinear mechanical behavior. There are materials to model irreversible deformation and temperature-dependent volume change in addition to elastic and viscoelastic materials.

4. Define the mechanisms that drive the stresses. Intrinsic stresses, thermal mismatch, material growth, lattice mismatch (silicon germanium), and densification are all used in the Sentaurus Process to perform this. In the linear elastic regime, all of these processes are additive. On other hand, they must be updated from the available stress history in the nonlinear regime.

The tensor constitutive equations are divided into dilatational component and deviatoric component. The material behavior in the case of a pure volume change is described by the dilatational component, which corresponds to the trace of the tensor. An arbitrary deformation but without changing the volume is described by the deviatoric component.

```
#Stress-rebalancing step to re-establish the stress equilibrium
and to conform the stress distributions to the new boundaries
pdbSet Mechanics EtchDepoRelax 1

#Trace all temperature ramps to model stress evolution
accurately pdbSet Mechanics StressHistory 1

#The stress tensor can be decomposed and the resulting
dilatational and deviatoric stress components can be saved
on nodes
pdbSet Mechanics decomposeStress 1

#Tin oxide is created and made to be like germanium
```

```
mater add name= SnO2 new.like= Germanium

#Specify the crystal properties for cubic SnO2
mater name= SnO2 cubic lattice.const= 5.175e-4

#pdbSet SnO2 Potential Permittivity 2.28
#pdbSet SnO2 KMC BandGap Eg0 3.6
#pdbSet SnO2 Potential Affinity 5.73

#Switches on the anisotropic elasticity model for SnO2
pdbSet SnO2 Mechanics Anisotropic 1

#The values of the three modulus parameters with respect to the
cubic crystal axis (stiffness tensor)
#For a cubic crystal, the anisotropic stress and strain relation
is completely defined when three independent modulus parameters
C11 , C12 , and C44 are specified
#The unit for these values is dyn/cm^2
#These are the values for SnO2 that will modelize the SnO2 film
(from materialsproject.org/materials/mp-697/)
pdbSet SnO2 Mechanics C11 187E10
pdbSet SnO2 Mechanics C12 56E10
pdbSet SnO2 Mechanics C44 56E10
```

Listing 4.11. Stress simulation

A set of stress-driving mechanisms is needed for every mechanical system to reach a stressed state. For this work the stress-inducing mechanisms is the stress rebalancing after etching and deposition. When materials are removed from or added to a structure, the related geometry and boundary changes cause physical stress distributions to alter. A stress-rebalancing step is required in simulations to re-establish the structure stress equilibrium and adapt the stress distributions to the new boundaries. After etching or deposition, a stress-rebalancing operation is launched by the command: *pdbSet Mechanics EtchDepoRelax 1*.
The fabrication history of a device structure, which consists of process steps at multiple temperatures and temperature ramps in between, determines the thermal residual stress in that structure. All temperature ramps should be traced to accurately model stress evolution. When the command *accurately pdbSet Mechanics StressHistory 1* is used, temperature gaps between process steps such as diffusion, deposition, and etching are identified and filled with instant stress rebalancing, solving for thermal mismatch strains and stresses.
When the command *pdbSet Mechanics decomposeStress 1* the stress tensor can be decomposed and the resulting dilatational and deviatoric stress components can be saved on nodes.
The tin oxide is generated and made to be like the germanium using the command *mater add name= SnO2 new.like= Germanium*. The germanium has a semiconducting behavior

just like the tin oxide and, moreover, for germanium the anisotropic elastic material model is available in the PDB. The command *mater name= SnO2 cubic lattice.const= 5.175e-4* specifies the lattice system as cubic for the crystalline SnO_2 as well as the lattice constant which is euqal to 5.175Å[11].
Sentaurus Process implements five different material models: viscoelastic materials, purely viscous materials, purely elastic materials, anisotropic elastic materials and plastic materials.
The following equation can be used to describe the stress and strain relationships in anisotropic elastic materials:

$$\sigma_i = C_{ij}\varepsilon_j \tag{4.20}$$

where C_{ij} is the component of the stiffness matrix, σ_i is component of the engineering stress and ε_j is the component of the engineering strain. The engineering strain $\varepsilon_j(j = 1, ...,6)$ corresponds to the strain-tensor components $\varepsilon_{xx}, \varepsilon_{yy}, \varepsilon_{zz}, \varepsilon_{xy}, \varepsilon_{yz}, \varepsilon_{xz}$ and the engineering stress $\sigma_i(i = 1, ...,6)$ corresponds to the stress-tensor components $\sigma_{xx}, \sigma_{yy}, \sigma_{zz}, \sigma_{xy}, \sigma_{yz}, \sigma_{xz}$.
The symmetric stiffness matrix C, in a coordinate system with axes aligned along the crystal axes, has the following nonzero components: $C_{11} = C_{22} = C_{33}$, $C_{12} = C_{23} = C_{13}$, $C_{44} = C_{55} = C_{66}$.
The stiffness tensor and the compliance tensor of cubic SnO_2 are reported in figure 4.21 [11].

Stiffness Tensor C_{ij} (GPa)

187	56	56	0	0	0
56	187	56	0	0	0
56	56	187	0	0	0
0	0	0	56	0	0
0	0	0	0	56	0
0	0	0	0	0	56

Compliance Tensor S_{ij} (pPa^{-1})

6.2	-1.4	-1.4	0	0	0
-1.4	6.2	-1.4	0	0	0
-1.4	-1.4	6.2	0	0	0
0	0	0	17.8	0	0
0	0	0	0	17.8	0
0	0	0	0	0	17.8

Figure 4.21. Stiffness tensor (left) and compliance tensor (right) of cubic tin oxide.

When three independent modulus parameters C_{11}, C_{12}, and C_{44} are specified, the anisotropic stress and strain relation is completely defined. The degree of anisotropy for a given material can be measured by the departure from unity of the ratio:

$$A = \frac{2C_{44}}{(C_{11} - C_{12})} \tag{4.21}$$

If the ratio A is equal to 1, the anisotropic model reduces to the isotropic model. The stiffness matrix C must be changed when the simulation coordinate axes do not coincide

with the crystal axes. Note that C is a rank-4 tensor in this case. The anisotropic elasticity model is disabled by default. The model is turned on with the following command: *pdbSet SnO2 Mechanics Anisotropic 1*.
The following commands can be used to define the values of these three modulus parameters with respect to the cubic crystal axis, which also show the default values for the crystalline SnO_2 (figure 4.21): *pdbSet SnO2 Mechanics C11 187E10*, *pdbSet SnO2 Mechanics C12 56E10*, *pdbSet SnO2 Mechanics C44 56E10*. The unit for these default values is dyn/cm^2. This model depends on the *wafer.orient* and *slice.angle* parameters specified in the *init* command.
Note that the element of the stiffness tensor are used in Sentaurus Process to simulate the stress while the element of the compliance tensor are used in the *.par* file of the SnO_2 to simulate the stress with Sentaurus Device.

4.2 Electrical modeling of single tin oxide nanowire device sensor

4.2.1 Polycrystalline tin oxide parameters

Most physical models depend on parameters that can be adjusted in a file given by *Parameter* in the *File* section on Sentaurus Device [14]:

```
File {
Parameter = <string>
...
}
```

Listing 4.12. File section on Sentaurus Device

The name of the parameter file conventionally has the extension *.par*.
The following parameter sets is used for SnO_2:

- Epsilon
- LatticeHeatCapacity
- Kappa
- Bandgap
- eDOSMass
- hDOSMass
- ConstantMobility

The following parameters are used in the intrinsic surface state trapping model.

Mobility

The constant mobility model is active by default in Sentaurus. It accounts only for phonon scattering and, therefore, it is dependent only on the lattice temperature:

$$\mu_{const} = \mu_L \left(\frac{T}{300K} \right)^{-\zeta} \tag{4.22}$$

where μ_L is the mobility due to bulk phonon scattering.
Figure 4.22 depicts the temperature dependence of mobility of polycrystalline tin oxide.

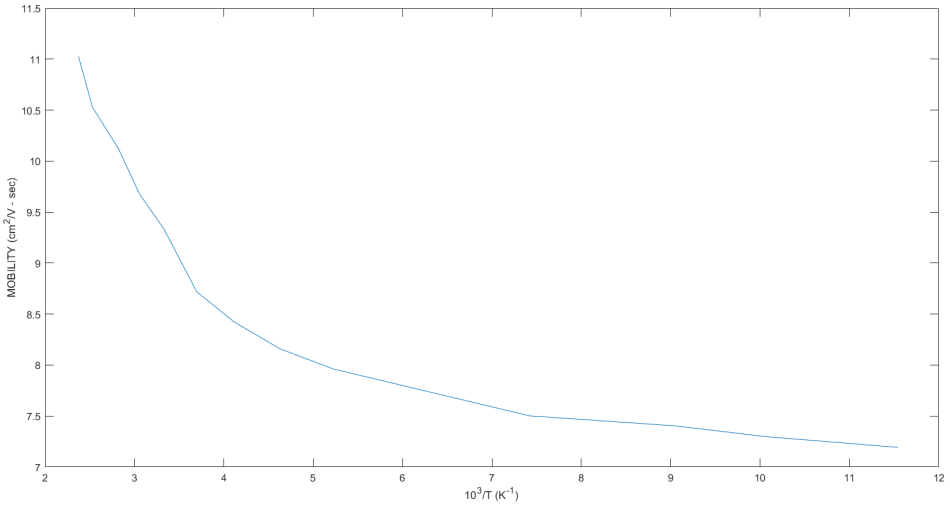

Figure 4.22. Temperature dependence of mobility.

The mobility decreases according to the relation:

$$\mu \propto T^{-3/2} \tag{4.23}$$

where T is the absolute temperature (K). Thus, on the parameter file of the SnO_2, mumax is set to 9.33 and exponent is set to 1.5.
Since the electrons are the majority carriers, the contribution of the holes to the total current is completely negligible, so the mobility value for holes does not matter.

Electron density

The electron density inside the polycrystalline SnO_2 nanowire is equal to 9.146×10^{24} m^{-3} [6]. To set the electron density the following commands are added into the sprocess command file.

```
# zfake is a fake variable for support.
```

```
sel z = 1 name=zfake store

# For  z>= 0 a uniform doping is assigned for the SnO2 nanowire.
The doping variable is named ArsenicNw.

sel z= " z >= 0.0  ? 9.146e18 : zfake " name=ArsenicNw SnO2 store

# The total doping variable is named AsActive (so that Sentaurus
can understand that it is an active dopant)

sel z= " ArsenicNw " name= AsActive store
```

Listing 4.13. Uniform doping in a specific region

The result is shown on figure 4.23.

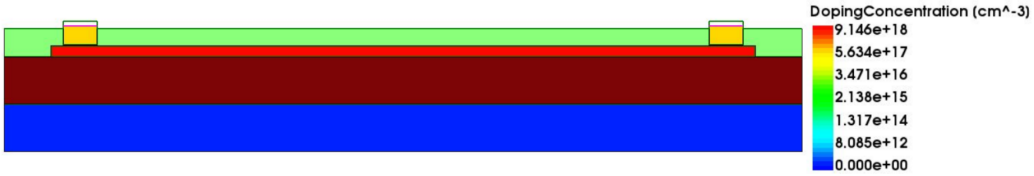

Figure 4.23. Structure doping concentration.

Band gap, electrical conductivity and electron affinity

The band gap (Eg0 on the parameter file) is grain size dependent and, since the grain size (50 nm) is comparable to the nanowire dimension, does not change with respect to the single crystal nanowire and it is still equal to 3.6 eV.
The electrical conductivity does not dramatically affect the electrical simulations and can be assumed to be the same as the monocrystalline one.
The electron affinity (Chi0 on the parameter file) is assumed to be equal to the monocrystalline one (5.73 eV) for simplicity. In reality, the electron affinity also changes with the number of adsorbed oxidizing gas (such as NO_2) molecules, so it varies dynamically.

4.2.2 Sentaurus Device

The electrical behavior of a single semiconductor device in isolation or numerous physical devices coupled in a circuit is numerically simulated by Sentaurus Device. The physical device equations that describe the carrier distribution and conduction mechanisms are used to calculate terminal currents, voltages, and charges. In the simulator, a real semiconductor device, such as a transistor, is represented as a virtual device, with its physical attributes discretized onto a nonuniform grid (or mesh) of nodes. A TDR file containing the following information is used to describe each virtual device structure in the Synopsys TCAD tool suite [14]:

- The device grid (or geometry) describes the various regions, including boundaries, material types, and the locations of any electrical contacts. It also contains the locations and connectivity of all discrete nodes.

- In the form of data associated with the discrete nodes, the data fields contain device properties such as doping profiles. A device simulated in 2D is assumed to have a third-dimensional thickness of 1 μm by default.

Sentaurus Device can solve three different types of simulations thanks to its mixed device and circuit capabilities: single device, single device with a circuit netlist, and multiple devices with a circuit netlist.In a typical device tool flow, the device structure is created by process simulation (Sentaurus Process). To simulate the electrical characteristics of the device Sentaurus Device is used. Finally, to visualize the output from the simulation in 2D and 3D Sentaurus Visual is used, and to plot the electrical characteristics Inspect is used [14].

2D structure

The 2D structure in figure 4.24 was used for electrical simulations mainly due to the shorter duration of the simulation times compared to the 3D case and because the results are almost the same as those of the 3D case, since the nanowire is almost uniform.
The green material covers the entire surface of the nanowire (purple) and serves to define the traps at the interface between it and the nanowire (thus emulating the presence of a gas to be detected). This material is an ideal insulator (essentially it is vacuum, dielectric constant 1).

Figure 4.24. Cross-section view of the final structure with surrounding gas-like material (green).

A remesh step was not necessary because a very dense mesh (1 nm) was defined from the outset for both the x and y directions. In figure 4.25 one can see how Sentaurus automatically refines the mesh at the interfaces between the various materials in order to obtain better results.

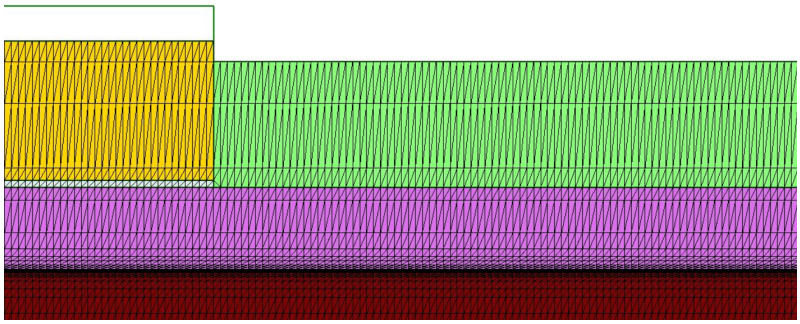

Figure 4.25. Result of the 2D meshing process.

Command file

The command file of Sentaurus Device is divided in six sections:

1. File section.
2. Electrode section.
3. Physics section.
4. Plot section.
5. Math section.
6. Solve section.

```
File
{
*INPUT FILES
Grid ="n5_presimulation_fps.tdr"
* physical parameters
Parameter = "sdevice.par"

*OUTPUT FILES
Plot = "n@node@_des.tdr"
* electrical characteristics at the electrodes
Current= "n@node@_des.plt"
}
```

Listing 4.14. File section

In total four files are used, two in input and two in output. The n5_presimulation_fps.tdr file contains the structure for which we want to simulate the electrical behavior while the sdevice.par file is used for the material parameter files. The two output files are used to save the structure after the electrical simulation (tdr file) and to save the electrical characteristics at the electrodes (plt file).

```
Electrode
{
{ name="source" Voltage=0.0 }
{ name="drain" Voltage=0.0 }
}
```

Listing 4.15. Electrode section

The electrode section is used to define contacts and their initial voltage, in this case 0V for both drain and source.

```
Physics
{
Temperature = 573
eQuantumPotential
EffectiveIntrinsicDensity( BandGapNarrowing(oldSlotboom) )
Mobility( DopingDep
        eHighFieldSaturation ( GradQuasiFermi)
        hHighFieldSaturation ( GradQuasiFermi)
        Enormal )
Recombination (
        SRH (DopingDep TempDependence)
        Band2Band(Model = NonLocalPath)
        )
}

Physics(MaterialInterface="SnO2/Anyinsulatorvac") {
  Traps (
*The energy of the center of the trap distribution is
Ec-EnergyMid
    (Acceptor Conc=1.191e13 Level EnergyMid=1 fromCondBand)
  )
}
```

Listing 4.16. Physics section

The physics section controls the physical behavior of the device during the electrical simulation. In particular, the temperature (573 K) and the traps are defined.
The trap type is *Acceptor*: traps are uncharged when unoccupied and they carry the charge of one electron when fully occupied. The keyword *Level* determines the energetic distribution of traps and select a single-energy level (N_0 for $E = E_0$). N_0 is set with the *Conc* keyword. For a Level distribution, Conc is given in cm^{-2} (for interface-wise specifications) and it is equal to 1.191×10^{13} cm^{-2} [6]. The energy of the center of the trap distribution,E^0_{trap} , is obtained from E_0 depending on the presence of the keyword *fromCondBand*: $E^0_{trap} = E_C - E_0 - E_{shift}$. E_0 is given in eV by EnergyMid and E_{shift} is zero (the default).
By increasing EnergyMid (moving away the energy level of the traps from Ec) what happens is that the probability of occupation of the traps increases. By increasing EnergyMid,

the traps move away from Ec, and being traps that act on the electrons in the conduction band (emptying the nanowires the bands fold and electrons in the conduction band are removed) moving it away from Ec we got that on average more traps will be occupied. Note that EnergyMid is a fitting parameter that would allow to emulate the experimental data on the occupation of the adsorption sites, in fact it acts on the probability of occupation of the traps.

```
Plot
{
eDensity hDensity eCurrent hCurrent
ElectricField eEnormal hEnormal
eQuasiFermi hQuasiFermi
Potential Doping SpaceCharge
eMobility hMobility eVelocity hVelocity
DonorConcentration AcceptorConcentration
Doping
BandGap BandGapNarrowing ElectronAffinity
ConductionBandEnergy ValenceBandEnergy
eQuantumPotential
Band2BandGeneration
}
```

Listing 4.17. Plot section

In Plot section are placed the data that are saved at the end of the simulation to the Plot file specified in File section.

```
Math
{
-CheckUndefinedModels
Extrapolate
* use full derivatives in Newton method
Derivatives
* control on relative and absolute errors
RelErrControl
* relative error= 10^(-Digits)
Digits=5
* absolute error
Error(electron)=1e8
Error(hole)=1e8
* numerical parameter for space-charge regions
eDrForceRefDens=1e10
hDrForceRefDens=1e10
Notdamped=50
* maximum number of iteration at each step
Iterations=100
ExitOnFailure
```

```
* solver of the linear system
Method=ParDiSo
Wallclock
NoSRHperPotential
}
```

Listing 4.18. Math section

The Math section contains all the commands necessary to perform the calculations of the equations used in the solve section.

```
Solve
{
coupled {Poisson}
coupled{ Poisson Electron Hole }

quasistationary (InitialStep = 0.01 MaxStep = 0.01 MinStep=1e-2
Goal {name= "drain" voltage = 2}
plot { range=(0, 2) intervals=1 }
){coupled { Poisson  Electron Hole }}

}
```

Listing 4.19. Solve section

Trap occupation

The electron occupation f^n of a trap is a number between 0 and 1, and changes due to the capture and emission of electrons [14]:

$$\frac{\partial f^n}{\partial t} = \sum_i r_i^n \tag{4.24}$$

$$r_i^n = (1 - f^n)c_i^n - f^n e_i^n \tag{4.25}$$

c_i^n denotes an electron capture rate for an empty trap and e_i^n denotes an electron emission rate for a full trap, respectively [14].
The time derivative vanishes for the stationary state and the occupation becomes [14]:

$$f^n = \frac{\sum c_i^n}{\sum (c_i^n + e_i^n)} \tag{4.26}$$

the net electron capture rate due to process k becomes [14]:

$$r_k^n = \frac{c_k^n \sum e_i^n - e_k^n \sum c_i^n}{\sum (c_i^n + e_i^n)} \tag{4.27}$$

Electrical simulation

The Solve section describes the simulation. The Coupled command is used to solve a set of equations. The drain voltage goes up to 2V.
The characteristic of the isolated sensor (without any traps at the interface) is depicted on figure 4.26 (blue) and the conductance in this case in equal to 1.64 × 10-4 S. When the traps at the interface are present the conductance decrease to 1.458 × 10-4 S as expected, figure 4.26 (red).
When the traps are active they accept electrons and create a positive space charge inside the nanowire; this is exactly what happened when the oxidizing gas molecules (such as NO_2) are adsorbed on the nanowire surface. As a consequence, the bands bend and the resistance increase.
Since the electron density is 9.146 x 10^{18} cm^{-3}, we can see on figure 4.27 that the nanowire (from -0.5 to -0.62) is fully depleted in the orange region as expected. Moreover, the conductance decreases so the model is working as expected. We expected that the region with the negative space charge was not inside the nanowire but only at the interface but that's reasonable because in reality since the molecules become negative ions when they are adsorbed on the nanowire surface (because they take one or two electrons each) so on the nanowire surface there is a negative charge.

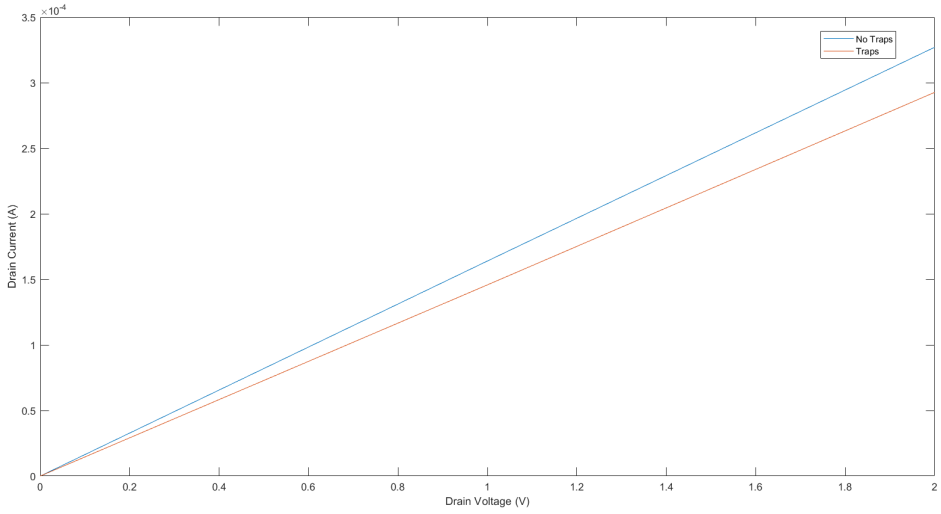

Figure 4.26. Characteristic of the isolated sensor versus the characteristic of the sensor when the traps are active.

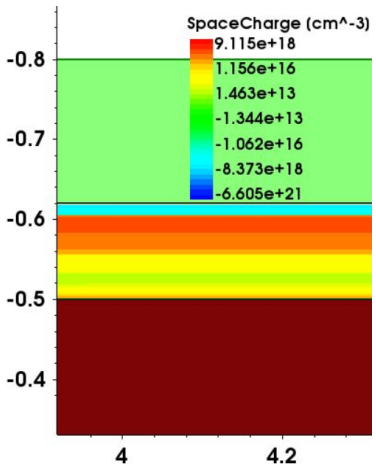

Figure 4.27. Space charge inside the nanowire.

Chapter 5

Conclusions

In this work, the fabrication process of a tin oxide nanowire sensor was simulated using Sentaurus TCAD and the electrical modelling for the polycrystalline tin oxide nanowire sensor was made.
The first part of this work was essentially a literature review of the semiconducting metal oxide gas sensors. Environmentally hazardous gases were introduced as well as the most common n-type and p-type metal oxide semiconductors. The general gas-sensing mechanisms were discussed in general and for the tin oxide sensors. The bottom-up and top-down fabrication process approaches of metal oxide nanowires were discussed. The vapor-liquid-solid growth and the RF magnetron sputtering and lift-off methods were presented.
The second part was instead focused on the fabrication process simulation and electrical modeling of tin oxide nanowire sensors. The RF magnetron sputtering and lift-off top-down method was considered. The physical models used by Sentaurus Topography 3D were discussed and the whole fabrication process simulation was explained in detail. Finally, the electrical modeling and the Sentaurus Device electrical simulation were discussed.

5.1 Future works

The response of a sensor in the case of oxidizing gas is defined as the ratio between resistance in the presence of the target on the resistance in an inert environment, the traps concentration can be changed until the desired response is found. In the simulation, the resistance can be changed in the presence of the target until the values obtained are the same as the experimental ones.
One can look for experimental data on which to do the fitting of the number of traps. It is possible to calculate exactly the concentration of traps (N_0, trap concentration) in a future work, because it is a complicated problem that requires considerations of chemistry or physics of the interfaces.

Bibliography

[1] N. Barsan, Cristian Simion, Thomas Heine, Suman Pokhrel, and U. Weimar. Modeling of sensing and transduction for p-type semiconducting metal oxide based gas sensors. *Journal of Electroceramics*, 25:11–19, 08 2010. doi: 10.1007/s10832-009-9583-x.

[2] Ajit Behera, Shampa Aich, and T. Theivasanthi. Chapter 8 - magnetron sputtering for development of nanostructured materials. In Sabu Thomas, Nandakumar Kalarikkal, and Ann Rose Abraham, editors, *Design, Fabrication, and Characterization of Multifunctional Nanomaterials*, Micro and Nano Technologies, pages 177–199. Elsevier, 2022. ISBN 978-0-12-820558-7. doi: https://doi.org/10.1016/B978-0-12-820558-7.00002-9. URL https://www.sciencedirect.com/science/article/pii/B9780128205587000029.

[3] Xianping Chen, Cell K.Y. Wong, Cadmus A. Yuan, and Guoqi Zhang. Nanowire-based gas sensors. *Sensors and Actuators B: Chemical*, 177:178–195, 2013. ISSN 0925-4005. doi: https://doi.org/10.1016/j.snb.2012.10.134. URL https://www.sciencedirect.com/science/article/pii/S0925400512011707.

[4] E. Comini. Metal oxides nanowires chemical/gas sensors: recent advances. *Materials Today Advances*, 7:100099, 2020. ISSN 2590-0498. doi: https://doi.org/10.1016/j.mtadv.2020.100099. URL https://www.sciencedirect.com/science/article/pii/S2590049820300461.

[5] Hong Ding, Shyam S. Dwaraknath, Lauren Garten, Paul Ndione, David Ginley, and Kristin A. Persson. Computational approach for epitaxial polymorph stabilization through substrate selection. *ACS Applied Materials & Interfaces*, 8(20): 13086–13093, 2016. doi: 10.1021/acsami.6b01630. URL https://doi.org/10.1021/acsami.6b01630. PMID: 27145398.

[6] Junhua Ding, Thomas J. McAvoy, Richard E. Cavicchi, and Steve Semancik. Surface state trapping models for sno2-based microhotplate sensors. *Sensors and Actuators B: Chemical*, 77(3):597–613, 2001. ISSN 0925-4005. doi: https://doi.org/10.1016/S0925-4005(01)00765-1. URL https://www.sciencedirect.com/science/article/pii/S0925400501007651.

[7] Owen C. Ernst, David Uebel, Stefan Kayser, Felix Lange, Thomas Teubner, and Torsten Boeck. Revealing all states of dewetting of a thin gold layer on a silicon surface

by nanosecond laser conditioning. *Applied Surface Science Advances*, 3:100040, 2021. ISSN 2666-5239. doi: https://doi.org/10.1016/j.apsadv.2020.100040. URL https://www.sciencedirect.com/science/article/pii/S2666523920300258.

[8] M. Ferreira, J. Loureiro, A. Nogueira, A. Rodrigues, R. Martins, and I. Ferreira. Sno2 thin film oxides produced by rf sputtering for transparent thermoelectric devices. *Materials Today: Proceedings*, 2(2):647–653, 2015. ISSN 2214-7853. doi: https://doi.org/10.1016/j.matpr.2015.05.090. URL https://www.sciencedirect.com/science/article/pii/S2214785315001613. 12th European Conference on Thermoelectrics.

[9] Vitaly Gurylev and Tsong Pyng Perng. Defect engineering of zno: Review on oxygen and zinc vacancies. *Journal of the European Ceramic Society*, 41(10):4977–4996, 2021. ISSN 0955-2219. doi: https://doi.org/10.1016/j.jeurceramsoc.2021.03.031. URL https://www.sciencedirect.com/science/article/pii/S0955221921001801.

[10] Haiping He. 2 - metal oxide semiconductors and conductors. In Zheng Cui and Ghenadii Korotcenkov, editors, *Solution Processed Metal Oxide Thin Films for Electronic Applications*, Metal Oxides, pages 7–30. Elsevier, 2020. ISBN 978-0-12-814930-0. doi: https://doi.org/10.1016/B978-0-12-814930-0.00002-5. URL https://www.sciencedirect.com/science/article/pii/B9780128149300000025.

[11] Kristin Persson. Materials data on sno2 (sg:205) by materials project, 7 2014.

[12] Gaurav Saxena and Roy Paily. Analysis of nanowire transistor based nitrogen dioxide gas sensor – a simulation study. *Sensing and Bio-Sensing Research*, 4:57–60, 2015. ISSN 2214-1804. doi: https://doi.org/10.1016/j.sbsr.2015.03.001. URL https://www.sciencedirect.com/science/article/pii/S2214180415000094.

[13] Synopsys. Sentaurus tcad industry-standard process and device simulators, 2012.

[14] Synopsys. *Sentaurus^{TM} Device User Guide*, Sept 2017. Version N-2017.09.

[15] Synopsys. *Sentaurus^{TM} Process User Guide*, Sept 2017. Version N-2017.09.

[16] Synopsys. *Sentaurus^{TM} Topography 3D User Guide*, Sept 2017. Version N-2017.09.

[17] M. Tonezzer and N.V. Hieu. Size-dependent response of single-nanowire gas sensors. *Sensors and Actuators B: Chemical*, 163(1):146–152, 2012. ISSN 0925-4005. doi: https://doi.org/10.1016/j.snb.2012.01.022. URL https://www.sciencedirect.com/science/article/pii/S0925400512000457.

[18] K. Wetchakun, T. Samerjai, N. Tamaekong, C. Liewhiran, C. Siriwong, V. Kruefu, A. Wisitsoraat, A. Tuantranont, and S. Phanichphant. Semiconducting metal oxides as sensors for environmentally hazardous gases. *Sensors and Actuators B: Chemical*, 160(1):580–591, 2011. ISSN 0925-4005. doi: https://doi.org/10.1016/j.snb.2011.08.032. URL https://www.sciencedirect.com/science/article/pii/S0925400511007556.

[19] Wikipedia contributors. Adsorption — Wikipedia, the free encyclopedia, 2022. URL https://en.wikipedia.org/w/index.php?title=Adsorption&oldid=1079407017.

[20] Qi-Hui Wu, Jing Li, and Shi-Gang Sun. Nano sno2 gas sensors. *Current Nanoscience*, 6:525–538, 10 2010. doi: 10.2174/157341310797574934.

[21] Na Zhang. Literature research report for lift-off method, 2006. for BME 390A, term project.